UNIVERSITÉ D'ORLÉANS

ÉCOLE DOCTORALE Énergie, Matériaux, Sciences de la Terre et de l'Univers

LPC2E

THÈSE

présentée par :

Nini BERGE

soutenue le : **21 décembre 2020**

pour obtenir le grade de : **Docteur de l'Université d'Orléans**

Discipline/Spécialité : **Sciences de l'Univers**

Terrestrial Gamma-ray Flashes and Associated Electromagnetic Emissions; from Radio to Gamma rays

THÈSE dirigée par :

CELESTIN Sébastien	Associate Professor, Université d'Orléans, France

RAPPORTEURS :

BLELLY Pierre-Louis	Directeur de Recherche, IRAP, CNRS, France
MARISALDI Martino	Associate Professor, University of Bergen, Norway

---

JURY :

ABBASI Rasha	Assistant Professor, Loyola University Chicago, USA
BLANC Elisabeth	Directeur de Recherche, DAM, CEA, France
PINÇON Jean-Louis	Chargé de Recherche, CNRS, LPC2E, France

Abstract

Terrestrial Gamma-ray Flashes (TGFs) are bright, sub-millisecond bursts of gamma rays originating in the electric fields of thunderstorms. TGFs are thought to be initiated by a process known as a Relativistic Runaway Electron Avalanche (RREA), but the exact seeding mechanism and general context behind the process remain debated. In this thesis, we use a range of modeling tools to explore several different aspects of TGFs and associated electromagnetic emissions. In doing so, we address some of the most recent research in the field of high-energy atmospheric physics.

As RREAs propagate, they leave a trail of low-energy electrons and positive and negative ions behind. These populations of charged particles will carry currents as they move in the thunderstorm electric field. We model the charged species left behind by the propagating RREA, and the resulting radio emissions in the context of injection of thermal runaway seed electrons by a lightning leader. We find that for certain initial conditions, these radio emissions match slow LF pulses that have previously been observed concurrently with TGFs. This confirms that the slow LF pulses are generated directly by the TGF source itself, as has been previously suggested. Slow LF pulses may therefore be used to infer characteristic properties of TGF sources.

Until recently, there were only a few ground-based observations of TGFs.

Since the Telescope Array in Utah, USA, started reporting detections of high-energy particles correlated with lightning, their number has greatly increased. Ground observations of TGFs represent a valuable addition to space-borne detectors. The proximity to the event and the ability to observe an event with several detectors may reveal new information about the production of TGFs. We study downward directed TGFs using Monte Carlo modeling of photon transport through the atmosphere. The Telescope Array-observed pulses of gamma rays spread over periods of a few hundred microseconds, with time structures of less than 10 μs. We predict such structures to be observable at satellite altitude, given sufficient time resolution. Additionally, we demonstrate how various source spectra would lead to different number of photons reaching ground, which impacts the conclusions one can draw using observational data.

As a TGF propagates, gamma rays will knock electrons free as they interact with the surrounding air. These electrons emit bremsstrahlung (here referred to as secondary photons), mainly due to collisions with the nuclei of air molecules. Some of this bremsstrahlung has sufficient energy to reach satellite altitude. The spectrum of secondary photons is dependent on the initial TGF's properties, and can be used to infer these from observations. Secondary photons are also a direct signature of the energy deposited into the atmosphere by TGFs. Because they are not easily separated from the photons of the TGF, we propose three measures to analyze results relating to secondary photon spectra. In this way, we are able to quantify properties of TGFs with different initial energy spectra and beaming geometry.

In this thesis, we demonstrate that the combination of multiple TGF-related effects of different nature can be a powerful tool to solve many of the open questions in high-energy atmospheric physics.

Résumé

Les flashs gamma terrestres (TGF) sont d'intenses bouffées de rayonnement gamma, de durées inférieures à la milliseconde, produits dans les champs électriques des nuages d'orage. Les TGF sont déclenchés par un processus connu sous le nom d'Avalanche d'Électrons Runaway Relativistes (RREA), mais le mécanisme exact de production et le contexte général derrière ce processus fait encore débat. Dans cette thèse, nous utilisons différents outils de modélisation afin d'explorer les divers aspects des TGF ainsi que des émissions électromagnétiques qui leur sont associées. Ce faisant, nous abordons un des sujets de recherche les plus récents dans le domaine de la physique atmosphérique des hautes énergies.

Lors de la propagation des RREA, des électrons de basse énergie ainsi que des ions positifs et négatifs sont produits. Ces particules chargées produisent des courants lors de leur mouvement dans le champ électrique de l'orage. Nous modélisons les espèces chargées produites par les RREA, et les émissions radio qui en résultent dans le contexte d'électrons runaway thermiques injectés par un leader d'éclair. Nous trouvons que pour certaines conditions initiales, ces émissions radio correspondent aux "slow LF pulses" qui ont été précédemment observés simultanément avec des TGF. Cela confirme que les slow LF pulses sont en fait générés directement par la source du TGF elle-

même, comme cela a été précédemment suggéré. Les slow LF pulses pourront ainsi être utilisés pour déterminer les propriétés caractéristiques des sources de TGF.

Depuis que le Telescope Array (Utah, États-Unis) commence à détecter de particules de haute énergie corrélées avec des éclairs, le nombre de détection depuis le sol a considérablement augmenté. Les observations de TGF depuis le sol représentent un outil complémentaire aux observations satellites. La proximité avec l'évènement et la possibilité d'observer un évènement avec plusieurs détecteurs pourraient révéler de nouvelles informations sur la production des TGF. Nous nous intéressons aux TGF inversés (dirigés vers le sol) en utilisant un modèle Monte Carlo de transport de photon dans l'atmosphère. Les pulses de rayonnement gamma détectés par le Telescope Array s'étendent sur des périodes de quelques centaines de microsecondes, avec des structures temporelles inférieure à 10 μs. Nous prédisons que de telles structures seraient observables aux altitudes de satellites, en supposant une résolution temporelle suffisante. D'autre part, nous démontrons comment différents spectres de sources de TGF mèneraient à différent nombres de photons atteignant le sol, ce qui impacte les conclusions qu'on peut tirer en utilisant les données observationnelles.

Lors de la propagation d'un TGF, le rayonnement gamma qui ionise l'air environnant, produisent ainsi des électrons libres. Ces électrons émettent un rayonnement bremsstrahlung (ici appelé photons secondaires), principalement dû aux collisions avec les noyaux des molécules de l'air. Une partie de ce rayonnement bremsstrahlung sera d'énergie suffisante pour atteindre l'altitude des satellites. Le spectre de ces photons secondaires dépend des propriétés initiales du TGF, et peut être utilisé pour caractériser ces dernières à partir des observations. Les photons secondaires sont également une signature directe de l'énergie déposée dans l'atmosphère par les TGF. Parce qu'ils ne sont pas facilement distinguables des photons du TGF, nous proposons trois mesures pour analyser les résultats liés aux spectres des photons secondaires. De cette façon, nous sommes capables de quantifier les propriétés de TGF de différents spectres initiaux et différentes géométrie de faisceaux.

Dans cette thèse, nous démontrons que la combinaison de divers effets de différentes natures liés aux TGF peut être un outil puissant pour résoudre nombre de questions ouvertes dans le domaine de la physique de l'atmosphère des hautes énergies.

Acknowledgments

I would first like to thank my thesis advisor, Sebastien Celestin, for his sage advice and great availability, as well as for the opportunities he has facilitated for collaborations and travel. I also thank my collaborators who were instrumental in the study presented in Chapter 3; Matthieu Garnung, Robert Marshall, Wei Xu, and Steven Cummer, as well as David Sarria for his input in the early stages of the project presented in Chapter 5. I would like to thank Kader Amsif, responsible for my thesis at CNES, for his support and for showing me TARANIS in person.

I thank the reviewers (Pierre-Louis Blelly and Martino Marisaldi) and the other members of my PhD committee (Rasha Abbasi, Elisabeth Blanc, and Jean-Louis Pinçon) for having agreed to evaluate this thesis.

A final thanks to my current and former colleagues and friends at LPC2E: Andrea Larosa, Anna Tkachenko, Claire Revillet, Matthieu Garnung (computer oracle and spider remover), Mélody Pallu (for all the French language help), Minna Myllys, Vamsee Jagarlamudi, and many others, who have been integral to my PhD experience.

My research has been funded by CNES in the framework of the TARANIS mission and the Région Centre-Val de Loire.

List of abbreviations

ASIM *Atmosphere-Space Interactions Monitor* (spaceborne instrument on the ISS)

AGILE *Astrorivelatore Gamma a Immagini Leggaro* (satellite)

BATSE *Burst And Transient Source Experiment* (spaceborne instrument on the CGRO)

CG *Cloud-to-Ground* (lightning)

CSDA *Continuous Slowing Down Approximation*

CGRO *Compton Gamma-Ray Observatory* (satellite)

CNES *Centre National d'Études Spatiales*

DC *Direct Current*

ESA *European Space Agency*

FT *Florida Institude of Technology*

IC *Intra-Cloud* (lightning)

IDEE *Instrument Détecteur d'Electrons Energétiques* (spaceborne instrument on TARANIS)

IME-BF *Instrument de Mesure du champ Électrique Basse Fréquence* (spaceborne instrument on TARANIS)

IME-HF *Instrument de Mesure du champ Électrique Haute Fréquence* (spaceborne instrument on TARANIS)

ISS	*International Space Station*
IMM	*Instrument de Mesure du champ Magnétique* (spaceborne instrument on TARANIS)
LF	*Low Frequency* (30 – 300 kHz)
LOFT	*Large Observatory For x-ray Timing*
MCP	*MicroCameras and Photometers* (spaceborne instrument on TARANIS)
RHESSI	*Reuven Ramaty High Energy Solar Spectroscopic Imager* (satellite)
RREA	*Relativistic Runaway Electron Avalanche*
TA	*Telescope Array*
TARANIS	*Tool for the Analysis of RAdiation from lightNing and Sprites* (satellite)
TASD	*Telescope Array Surface Detector*
TEB	*Terrestrial Electron Beam*
TGF	*Terrestrial Gamma-ray Flash*
UHF	*Ultra-High Frequency* (300 MHz – 3 GHz)
XGRE	*X-ray, Gamma-ray and Relativistic Electron experiment* (spaceborne instrument on TARANIS)

Contents

Chapter 1

Introduction

1.1 Terrestrial gamma-ray flashes

Terrestrial gamma-ray flashes (TGFs) are bursts of high-energy photons of sub-millisecond duration originating in thunderstorms, bright enough to be routinely observed from space. They were discovered by *Fishman et al.* [1994] using the BATSE instrument aboard the Compton Gamma Ray Observatory. Since then, TGFs have been detected by several other satellites, notably RHESSI [*Smith et al.*, 2005], Fermi [*Briggs et al.*, 2010], AGILE [*Marisaldi et al.*, 2010], and the instrument ASIM mounted on the International Space Station [*Østgaard et al.*, 2019]. The study of TGFs, as well as their associated electromagnetic emissions and other high-energy phenomena originating in thunderstorms, comprise the rapidly growing field of high-energy atmospheric physics [*Dwyer et al.*, 2012].

The energy spectrum of TGFs suggests that they originate as bremsstrahlung from Relativistic Runaway Electron Avalanches (RREA) [*Dwyer et al.*, 2012], believed to be either formed in the large-scale thundercloud electric field [e.g., *Dwyer*, 2008], or in smaller scale inhomogeneous fields produced by lightning leaders [e.g., *Celestin and Pasko*, 2011]. As a result of the RREA process and subsequent bremsstrahlung, the initial photon spectrum of TGFs follows an exponential distribution with a cutoff energy at 7.3 MeV [e.g., *Coleman and Dwyer*, 2006]. TGFs observed from space are considered to be produced between 10 and 15 km altitude [*Xu et al.*, 2012; *Cummer et al.*, 2014], in association with intra-cloud lightning activity [*Stanley et al.*, 2006], more specifically to the initial stages of upward negative leaders [e.g., *Cummer et al.*, 2015; *Lu et al.*, 2010; *Shao et al.*, 2010].

In this thesis, we aim to answer a set research questions related to how modeling TGFs and associated electromagnetic emissions can be used to improve our understanding of the context of their production.

- Chapter 3 explores whether leader-based TGF generation models are compatible with observations of radio emissions known as slow LF pulses. And if they are, what can they teach us about TGF source properties?
- Chapter 4 is a study of how ground-based detections of downward TGFs using large detector arrays can be used to constrain the initial beaming geometry and energy spectrum.
- Chapter 5 poses the question of how we can use the population of secondary X-rays created during TGF propagation to better understand the properties of the TGF source.

The future space mission TARANIS funded by the French space agency (CNES) is partly dedicated to the study of TGFs. TARANIS should be the first space mission to combine optical, particle, and radio instruments.

Optical measurements will be done by photometers and cameras dedicated to the observation of transient luminous events and lightning (the instrument MCP). Particle detectors capable of discriminating electrons from photons (XGRE) and electron detectors (IDEE) will play a critical role in the identification of TGFs and their by-products. But the most interesting innovation of TARANIS is the combination of these detectors and a unique suite of radio instruments measuring electric fields from DC to 35 MHz (the instruments IME-BF [DC, 1MHz] and IME-HF [100 kHz-35 MHz]), and magnetic fields from 5 Hz to 1 MHz (IMM).

The results reported in this thesis, focused on the electromagnetic emissions from TGFs from radio to gamma rays, will be of great importance to the scientific return of TARANIS, as well as improving our general knowledge about these phenomena.

This chapter will provide an overview of the leading theories for the mechanisms of TGF production, followed by introductions to the work presented in the different chapters of this thesis. A summary of the main findings of the different chapters is provided in the conclusion (Chapter 6).

1.2 TGF production mechanisms

1.2.1 Runaway electrons

When electrons with a large kinetic energy move in sufficiently high electric fields in air, they will gain more energy from the field than they lose through interactions with the surrounding air. In this situation, the electron will continue gaining more and more energy, known as the electron "running away”, a mechanism first described by *Wilson* [1924].

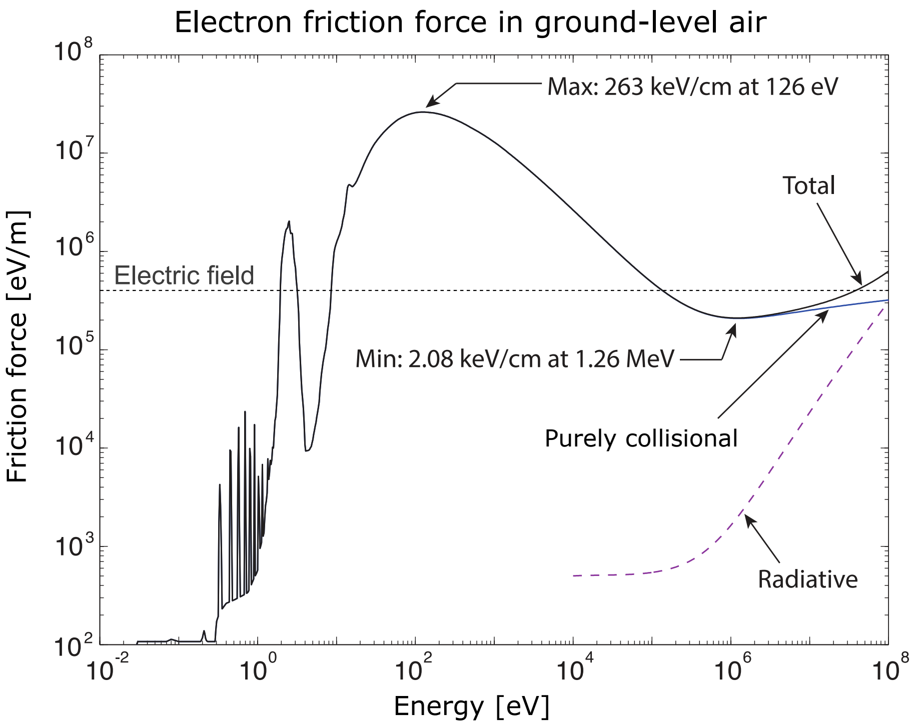

Fig. 1.1: The stopping power, or frictional force, experienced by an electron moving in an electric field in air. The stopping power results from energy lost through collisions (collisional friction) and bremsstrahlung (radiative part).

The stopping power, in practice a frictional force, experienced by an electron moving in air is shown as a function of energy in Figure 1.1. The electric field in which an electron can run away has to be stronger the break-even field, $E_t \simeq 2.1$ kV/cm (Figure 1.1). In order to run away, an electron must have an energy high enough so that it reaches the point where the frictional force curve in Figure 1.1 intersects the force applied by the surrounding electric field (the force corresponding to an electric fields is shown as a horizontal line in the figure). An electric field above the critical value $E_c \simeq 260$ kV/cm will allow all electrons to run away — a process known as thermal runaway, further discussed in Section 1.2.4.

An electron of sufficient energy to run away in a given field is known as a seed electron. *Wilson* [1924] suggested that these seeds would have to come from cosmic rays, or from radioactive decay. This cannot alone explain fluxes of X-rays measured from thunderstorms [*McCarthy and Parks*, 1992], and much less TGFs, which have been estimated to require $10^{16} - 10^{18}$ relativistic runaway seed electrons [*Dwyer and Smith*, 2005].

1.2.2 Relativistic runaway electron avalanches

A mechanism which would increase the flux of runaway electrons was proposed by *Gurevich et al.* [1992]. If electron-electron (Møller) scattering is taken into account, each seed electron undergoing the runaway process can create an avalanche of relativistic electrons, given an electric field above a threshold value. In essence, each runaway electron can knock other electrons off molecules from the surrounding air. If the new free electron is sufficiently energetic, it can then also run away, knock off more electrons, and as such propagate an avalanche of runaway electrons. The process is aptly known as a Relativistic Runaway Electron Avalanche (RREA).

The threshold field for a RREA to occur is $E_{th} = 2.84 \cdot 10^5$ V/m. This field magnitude is similar to the peak electric field values measured in thunderstorms [*Rakov and Uman*, 2003; *Marshall et al.*, 1995].

The number of runaway electrons in a RREA, N_{RREA}, is dependent on the initial number of seed electrons, N_0. In a region with a homogeneous electric field of length L, the final number of runaway electrons is given by *Dwyer*

[2003] as

$$N_{RREA} = N_0 \cdot e^{L/\lambda} \tag{1.1}$$

where $\lambda \simeq 7300$ kV / (E – 276 kV/m) is the characteristic length of the avalanche for fields greater than 3 kV/m, and $\lambda \simeq 5100$ / (E - 285 kV/m) for lower fields [*Coleman and Dwyer*, 2006].

Despite the multiplication of runaway electrons introduced by the RREA, the number of electrons is not high enough to explain TGFs if the seeding mechanism relies solely on cosmic rays, even in the case of RREAs seeded by exensive air showers [*Dwyer et al.*, 2008]. In the following subsections, we present two proposed mechanisms for further amplification of the numbers – relativistic feedback (Section 1.2.3) and thermal runaway (Section 1.2.4).

1.2.3 Relativistic feedback

The theory of relativistic feedback was first presented by *Dwyer* [2003]. As the electrons of a RREA are deflected by molecular nuclei, they will emit high-energy photons as bremsstrahlung. Some of these photons will be emitted or scattered in a backwards direction compared to the the RREA. Such a photon could then travel back to the source region of the RREA, where they might undergo Compton scattering or photoelectric absorption, and in this way provide new seed electrons for the RREA. Additionally, photons of sufficient energy can pair produce, creating a positron, which could travel along the electric field in the opposite direction of the electrons. A positron like this could provide additional seed electrons through Bhahba scattering if it reaches the source region, producing new RREAs.

Dwyer et al. [2012] provide a diagram of the mechanisms of runaway electrons, RREAs, and relativistic feedback, including the electron multiplication factor involved in each step (Figure 1.2). The number of electrons after each avalanches is modified by a feedback factor γ. The magnitude of this factor determines the behavior of the feedback. For $\gamma < 1$, the number of electrons per avalanche will increase by a simple factor. As γ approaches one, the number of runaway electrons caused by feedback will far exceed the number from the original seed electrons. For a feedback factor $\gamma > 1$, the increase of electrons in each avalanche will become exponential. In such a case, the large amount of resulting ionization will lead to a current discharging the system [*Dwyer*, 2003; *Dwyer et al.*, 2012].

1.2.4 Thermal runaway

The models presented for runaway avalanches in previous sections have all been dependent on having high-energy electrons seeded by cosmic rays, or other external sources. An alternative to this is that thermal electrons could be accelerated in the high electric fields produced by streamers — filamentary discharges propagating the channel of ionized air (named the leader) necessary to the propagation of a lightning discharge. In a small region at the streamers' head, the electric field can presumably reach amplitudes above the critical electric field E_c, shown in Figure 1.1. In this case, low energy, non-relativistic electrons can run away, serving as seeds for large numbers of relativistic electrons. The concept is illustrated in Figure 1.3. It has been shown that sufficient fluxes of electrons to account for the number of gamma-rays in a TGF can be created this way [e.g., *Celestin et al.*, 2015]. It is

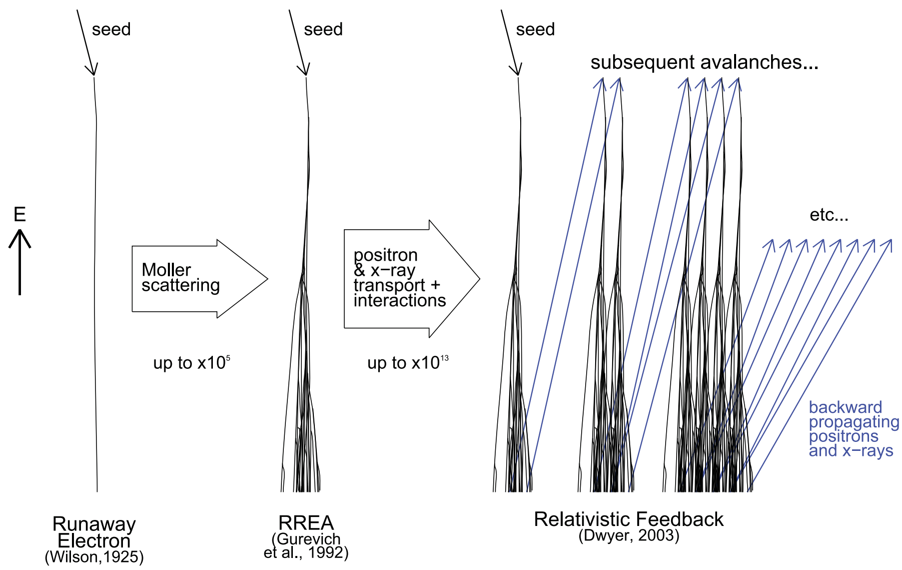

Fig. 1.2: A sketch of the concepts of runaway electrons, RREAs, and relativistic feedback, with the multiplication factors between them. This figure is from *Dwyer et al.* [2012].

possible that the different TGF production mechanisms act in concert.

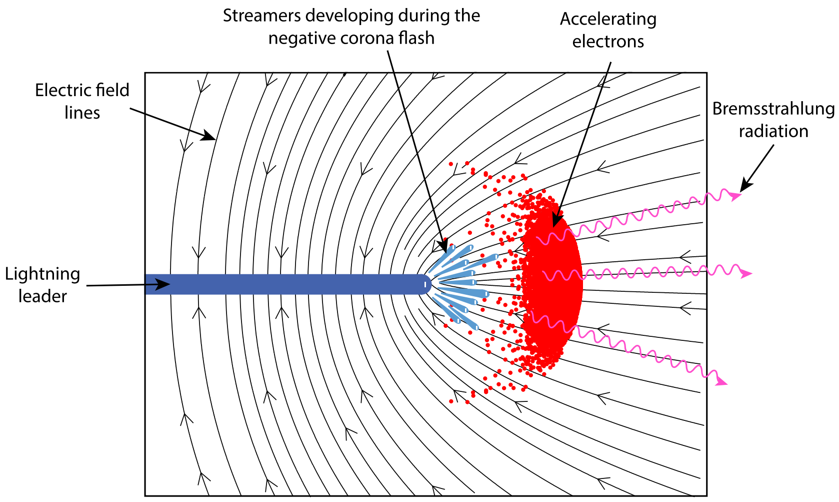

Fig. 1.3: Illustration of runaway electrons produced in front of a lightning leader and propagating in the leader electric field. From *Celestin et al.* [2015].

The energy spectrum of photons created by this process depends on the potential drop at the tip of the lightning leader. *Celestin et al.* [2015] showed that a lower potential leads to a softer spectrum, while a high potential drop ($\gtrsim$ 100 MV) gives an energy spectrum and photon count similar to that obtained using an exponential spectrum with a cutoff at 7.3 MeV. Such spectra are used as the initial spectra in the modeling done in Chapter 4.

1.3 Radio emissions from TGF sources

While studies that link satellite observations of TGFs to their parent lightning have relied on radio observations of said lightning, some specific radio signatures have been linked directly to TGF activity. Most notably Energetic In-cloud Pulses (EIPs) [e.g., *Lyu et al.*, 2016] and so-called slow low-frequency (LF) pulses. In this work, we will focus on the latter. Slow LF pulses were first reported by *Cummer et al.* [2011], with evidence suggesting them to be a direct signature of TGF production. This idea was further explored by *Dwyer and Cummer* [2013], where they use an analytical approach to calculate the expected radio emissions from TGF sources.

As the RREAs at a TGF's source (introduced in Section 1.2) propagate, they leave a trail of low-energy electrons and positive and negative ions behind. These populations of charged particles will carry currents as they move in the thunderstorm electric field. In Chapter 3, we will use a multifluid plasma model (described in Section 2.2.1) to find the current generated by ions and low energy electrons left behind a propagating RREA from first principles. The model handles the movement of charged species and the basic chemical processes they experience. It also allows self-consistent calculation of the electric field, thereby taking the non-linearity of the system into account. We then compare the results with measurements of slow LF pulses that have previously been observed concurrently with TGFs [*Pu et al.*, 2019]. We find that for certain initial conditions, the modeled radio emissions match the slow LF pulses. This confirms that the slow LF pulses are in fact generated directly by the TGF source itself, confirming previous suggestions using a different TGF production model. Slow LF pulses may therefore potentially be used to infer characteristic properties of TGF sources.

1.4 Downward directed TGFs

As mentioned in Section 1.1, there have been numerous satellite missions observing TGFs, compiling catalogs of thousands of events. But until recently, there were only occasional ground-based observations of TGFs. Two cases from rocket-triggered lightning [*Dwyer et al.*, 2004; *Hare et al.*, 2016], as well as two cases in association with negative cloud-to-ground (CG) lightning [*Dwyer et al.*, 2012; *Tran et al.*, 2015], had been observed in Florida, USA. Gamma-ray flashes have also been observed from ground during Japanese winter thunderstorms [*Enoto et al.*, 2017; *Smith et al.*, 2018]. While the observations by *Dwyer et al.* [2004]; *Dwyer et al.* [2012]; *Enoto et al.* [2017] and *Hare et al.* [2016] were made by several detectors simultaneously, the total number of photons received was limited, and the events are few and far between.

The number of ground observations of gamma-ray flashes from thunderstorms increased significantly as unusual observations correlated to lightning activity were reported from the Telescope Array (TA) in Utah, USA [*Abbasi et al.*, 2017, 2018]. The TA is a cosmic ray observatory that has an instrument of more than 500 scintillation detectors in a square grid with 1.2 km spacing called the Telescope Array Surface Detector (TASD). The observed events originate less than 5 km above ground level, and are correlated with the downward propagation of negative leaders. The large detector grid of the TASD gives an unusual advantage in observing TGFs from the ground — each event is registered across several detectors, giving a much clearer picture of the spatial and temporal shape of the signal than what single observation points are capable of. An example of such an event can be seen in Figure 1.4.

Ground observations of TGFs represent a valuable addition to space-borne detectors. The proximity to the event and the ability to observe an event with several detectors may reveal new information about the production of TGFs. To better be able to interpret observations such as those made by the TA, we model downward-directed TGFs using a Monte Carlo model of photon transport through the atmosphere. The TGFs are considered to be beamed downwards, i.e., produced by electrons accelerated in the direction of negative cloud-to-ground (-CG) lightning. Our aim is to quantify how differences in time structure, geometry, and energy spectrum of the initial gamma-ray flash present in ground-based observations. *Abbasi et al.* [2018] observed time structures consisting of 10 μs pulses spread over a few hundred microseconds. We find that such structures should also be observable by satellites, given sufficient time resolution. The detector grid of the TASD gives unprecedented information about the geometry of TGFs. However, atmospheric effects cause distortion of the initial beam shape. To resolve this, we define a parameter space from the observed photons' position, which can uniquely identify most possible geometries of the initial TGF beam. We also find that the number of photons reaching ground, as well as the shape of their energy spectra, strongly depends on the initial spectrum of the TGF. The results of this study are presented in Chapter 4.

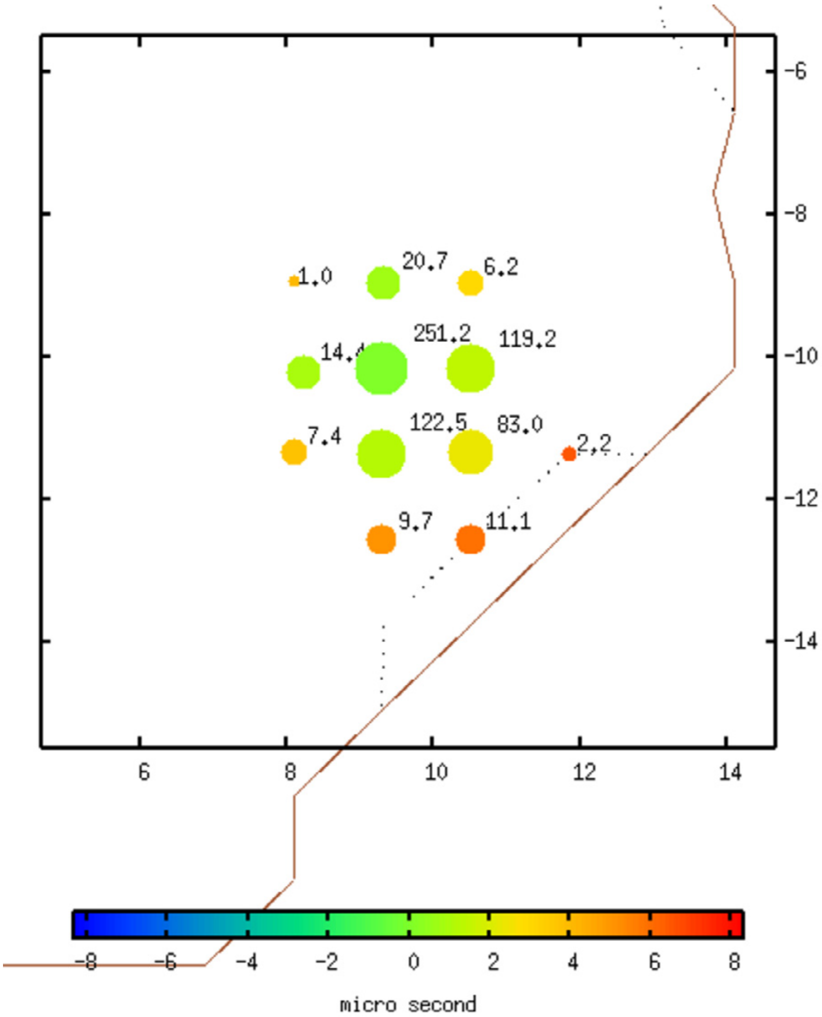

Fig. 1.4: A map of a gamma-ray detection done at the TA by *Abbasi et al.* [2017]. Each point corresponds to one detector in the array, with the point size referring to the number of hits in the detector, and the color to the timing. The brown line marks the edge of the area of the TA. Figure from *Abbasi et al.* [2017].

1.5 Secondary particles generated during TGF propagation

1.5.1 Secondary electrons

As the gamma-rays of a TGF propagate, they interact with the surrounding air. The most important interactions between gamma-rays and air molecules are Compton scattering, photoelectric absorption, and electron-positron pair production. Their relative rate of occurence at different energies can be seen in Figure 2.2.

The result of each of these interactions is the introduction of a free electron (and a positron, in the case of pair production), see Figure 1.5. We call these electrons *secondary electrons* throughout this work, to separate them from the electrons of the RREA at the source of the TGF.

Most of these electrons will quickly slow down and be absorbed in the atmosphere, making them a source of energy deposited into the atmosphere by TGFs. But, because the electrons often only move a few meters in the atmosphere before stopping, they are difficult to observe directly. The majority of these electrons can then only be observed by the effects they cause. It has for example been shown that the molecular excitation they cause may emit observable optical emissions [*Xu et al.*, 2017].

Some of the secondary electrons may also become trapped, spiraling around geomagnetic field lines. For certain configurations of the thundercloud electric field and the geomagnetic field, trapped electrons of sufficient energy may travel long distances without losing their energy. Such electrons are known as Terrestrial Electron Beams (TEBs), and have been observed by satellites [e.g., *Dwyer et al.*, 2008].

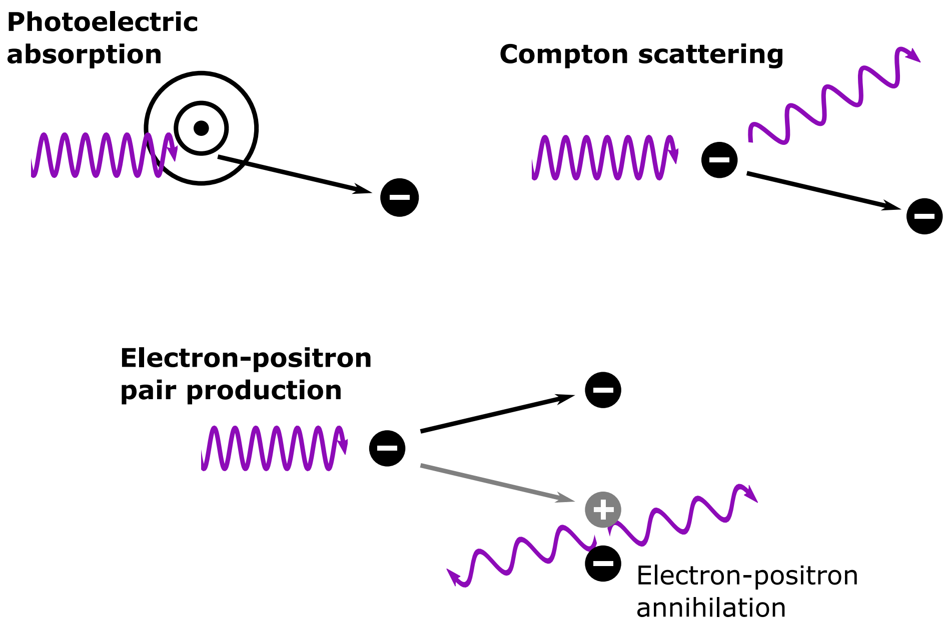

Fig. 1.5: Diagram illustrating collision processes taken into account in our modeling of photon transport: photoelectric absorption, Compton scattering, and electron-positron pair production. These are the main interactions TGF photons undergo as they propagate through the atmosphere. Photons are represented by purple lines, while electrons and positrons are black and grey circles, respectively.

1.5.2 Secondary photons

As the secondary electrons lose energy and slow down, they will emit photons through bremsstrahlung. Some of these photons will have a high enough energy that they can propagate and reach satellite altitude. We call these (and only these) photons *secondary photons*, as opposed to the primary photons of the original TGF. An argument can be made that photons produced by electron-positron annihilation as a result of pair production could also be called secondary photons, however, we here use the term exclusively for bremsstrahlung from secondary electrons. A sketch of the creation of secondary photons can be seen in Figure 1.6.

These secondary photons then represent another direct signature of the secondary electrons, and by extension of the energy deposited into the atmosphere by the TGF.

In Chapter 5, we describe how the secondary photons relate to the primary TGF. We demonstrate how the relationship of the two photon populations vary with the initial conditions of the TGF, and suggest some measures that can be applied to the resulting energy spectrum to obtain information about the TGF source.

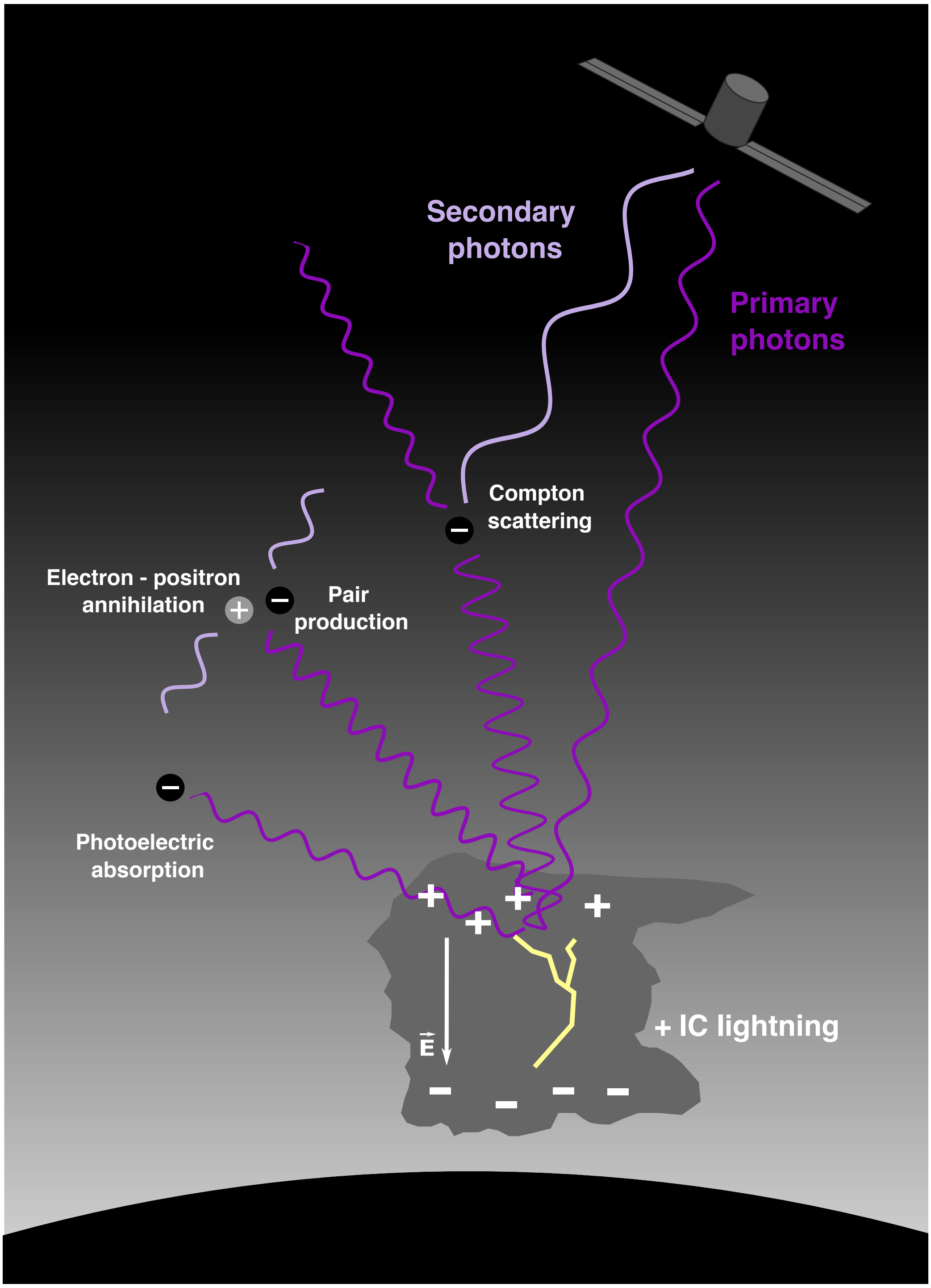

Fig. 1.6: A sketch of the propagation of a TGF and resulting particle interactions.

Chapter 2

Methods

This chapter gives an overview of the methods used throughout this thesis. Section 2.1 describes the Monte Carlo model for photon propagation and generation of secondary particles, which is used to obtain the results in Chapters 4 and 5. Section 2.2 describes the multiplasma fluid model and means for radio propagation used in Chapter 3.

2.1 Modeling TGF propagation

2.1.1 Photon propagation

We use a Monte Carlo model to propagate individual photons through the atmosphere in order to simulate the behavior of TGFs. The model is based on that presented in *Østgaard et al.* [2008].

Each photon is given an initial energy, position, and velocity, following pre-

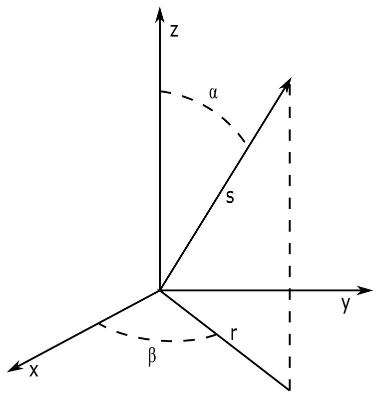

Fig. 2.1: Sketch of the geometry of photon propagation. Here, z represents the vertical, and x and y make the horizontal plane. Based on *Østgaard et al.* [2008].

determined distributions representing the energy spectrum and geometry of the TGF at its source. We then determine a path length, s, that the photon travels before it undergoes an interaction. The path length is given by *Østgaard et al.* [2008] as

$$s = \frac{-1}{a\cos(\alpha)} \ln\left[1 + \frac{\ln(1-R)a\cos(\alpha)}{\mu_{total}\rho_z}\right] \tag{2.1}$$

where the angle α is illustrated in Figure 2.1, R is a random number, and a is the coefficient in the exponential expression of the atmospheric density, ρ_z, given as

$$\rho_z = \rho_0 e^{-az} \tag{2.2}$$

In this manuscript, we assume an atmospheric composition of 80% N_2 and 20% O_2. The probability of interaction is represented by a coefficient for interaction $\mu_{total} = \mu_{absorption} + \mu_{Compton} + \mu_{e^-e^+}$, made up of the coefficients for each interaction — photoelectric absorption, Compton scattering, and electron-positron pair production, respectively. The type of interaction is then determined from the relative probabilities at a certain energy, as can be seen in Figure 2.2. The interaction coefficients are given by the cross sections of the three interactions at the relevant energy. The probability for one given interaction, k, is given by $P_k = \mu_k/\mu_{total}$. We use cross sections for Compton scattering and pair production from the NIST Standard Reference Database of photon cross sections (XCOM) [*Berger et al.*, 2010]. For Compton scattering, the energy of the scattered photon, γ', and its scattering angle, θ, is calculated using the equations given by *Lehtinen* [2000]:

$$\gamma' = \frac{\gamma}{1 + sR + (2\gamma - s)R^3} \quad , \quad s = \frac{\gamma}{1 + 0.5626\gamma} \tag{2.3}$$

$$\theta = \cos^{-1}\left(1 + \frac{1}{\gamma} - \frac{1}{\gamma'}\right) \tag{2.4}$$

where R is a uniformly distributed random variable between 0 and 1, and $\gamma = E/mc^2$ normalized to the electron rest energy.

For photoelectric absorption, we use the formulation for the cross section given by [*Lehtinen*, 2000, Section 3.2.2]. We keep track of each photon until it reaches satellite altitude, the ground, or until its energy falls below 10 keV.

When a photon collision occurs, the energy-momentum conservation allows to obtain the direction of the secondary electron (as well as that of the positron in the case of an electron-positron pair production). We also have the option of saving the information of the electrons created during these

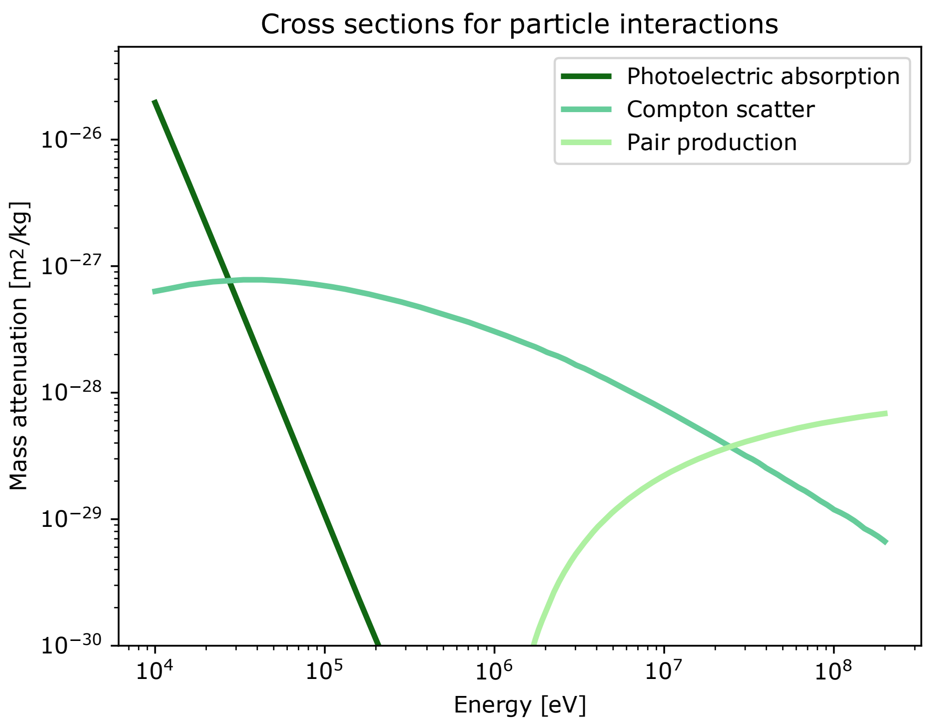

Fig. 2.2: Cross sections of the different particle interactions for different energies. Compton scattering dominates in the middle part of the energy range of TGFs, while photoelectric absorption and pair production take over for low and high energies, respectively.

interactions.

Throughout this work, we use an initial exponential spectrum with a cutoff energy at 7.3 MeV commonly associated with RREAs [*Coleman and Dwyer*, 2006; *Dwyer*, 2008], as well as spectra associated with different leader potential drops [*Celestin et al.*, 2015].

For the inital beaming geometry of the TGF, we can either use a point source, or photons distributed over a volume of space. In this work, the initial photon velocities are distributed uniformly within a cone-shaped beam. The source altitude of the TGF can also be set. We typically use 12 km for upward TGFs [*Xu et al.*, 2012; *Cummer et al.*, 2014], and 3 km for downward TGFs [*Abbasi et al.*, 2017], unless otherwise specified.

2.1.2 Bremsstrahlung

Secondary electrons are produced during the propagation of TGF photons through the atmosphere. These electrons primarily emit bremsstrahlung when they interact with the nuclei of nitrogen and oxygen molecules. We need to estimate the dynamics of secondary electrons produced in the atmosphere in order to quantify the amount and characteristics of this secondary emission. We make the assumption that electrons are continuously slowing down. We derive the friction force using the Bethe formula with a mean excitation potential of $I = 85.7$ eV, typical for the Earth's atmosphere [*Berger et al.*, 2016]. The equation of motion of electrons is solved numerically in the continuous slowing down approximation (CSDA). The energy spectrum of the bremsstrahlung photons is obtained by finding the energy of the electron at each time step of the simulation, and evaluating the Born approximation of the singly-differential cross section for bremsstrahlung emission.

In this way, we create a lookup table of the probability distributions of bremsstrahlung of different energies to occur for each electron energy. We can then use Monte Carlo sampling to quickly draw the energy and amount of bremsstrahlung emitted by an electron using these distributions.

The bremsstrahlung photons are considered to be produced in the same direction as the slowing down electron. For simplicity, positrons are assumed to follow the same dynamics as electrons when they slow down in the atmosphere, and to produce bremsstrahlung in the same way electrons do.

2.1.3 Secondary photons

In order to obtain the energy spectra and positions of secondary photons at satellite altitude, we first run the photon propagation code described in Section 2.1, collecting all electrons created during the propagation, conserving their position and velocity. Using this electron population, we then apply the method of Section 2.1.2 to create a population of secondary photons. The secondary photons are then propagated using the photon propagation model.

2.2 Modeling radio emissions from TGF sources

2.2.1 Fluid model

As a RREA progresses through air, it leaves behind a trail of positive ions and low energy electrons. We model their transport using a modified multi-fluid plasma model similar to those described in e.g., *Bourdon et al.* [2007] and *Ihaddadene and Celestin* [2015], which were originally designed for modeling streamer discharges. The model is based on solving the drift-diffusion equations for the charged species, coupled with Poisson's equation:

$$\frac{\partial n_e}{\partial t} + \nabla \cdot n_e \vec{v_e} - D\nabla^2 n_e = S^+_{ph} - S^-_e + S_{RREA} \tag{2.5}$$

$$\frac{\partial n_p}{\partial t} + \nabla \cdot n_p \vec{v_p} = S^+_{ph} + S^+_p + S_{RREA} \tag{2.6}$$

$$\frac{\partial n_n}{\partial t} + \nabla \cdot n_n \vec{v_n} = S^+_n \tag{2.7}$$

$$\nabla^2\Phi = -\frac{q}{\epsilon_0}(n_p - n_n - n_e) \tag{2.8}$$

where n, $\vec{v}$, D, and Φ are the number density, drift velocity, diffusion coefficient, and electric potential, respectively. The subscripts e, n, and p represent electrons, negative ions, and positive ions, respectively. S^+ and S^- represent the rates of production by electron impact and electron loss by attachment. Ion diffusion is neglected due to the timescales relevant to this study. The model is electrostatic, and as such does not include relativistic effects. Using this model, the densities control the electric field, which impacts the source terms, S, and the further transport of particles. The modeled scenario begins with the injection of thermal seed runaway electrons by a leader into an ambient electric field. As such, a large number of electrons (around 10^{15}, but this parameter is varied in different simulations) are injected into an electric field of about 1.3 times the RREA threshold field, extending over the first 4 km of a 6 km long simulation domain.

We have added a term for the production rate of electrons and positive ions due to the RREA, S_{RREA}, to the original model. The densities of positive ions, n_p, and electrons, n_e, created by a single RREA at location $z(t)$ can be expressed as:

$$n_p(z(t)) \simeq n_e(z(t)) = \frac{\alpha N_{run}(t)}{\pi \cdot R_D^2} \tag{2.9}$$

where R_D is the avalanche radius, $1/\alpha$ is the ionization mean free path ($\alpha \simeq$ 1500 m^{-1} at 12 km [e.g., *Dwyer and Babich*, 2011], and $N_{run}(t) = N_0 \cdot e^{\xi(t)}$ is the number of runaway electrons, with N_0 as the initial number of runaway electrons, and $\xi(t)$ the number of avalanche lengths depending on the RREA history.

$$\xi(t) = \int_0^t \nu_{run}(t')dt' = \int_0^t \frac{v_{RREA}}{\lambda(E(z(t')))}dt' \tag{2.10}$$

where ν_{run} is the runaway electron production frequency, $v_{RREA} \simeq 0.89$ c is the mean propagation speed of the RREA, and λ is the runaway avalanche characteristic length [*Coleman and Dwyer*, 2006].

The radius of the avalanche at a certain time can be estimated by:

$$R_D(t) = \sqrt{\frac{\beta D}{v_{RREA}} z(t) + R_0^2} \tag{2.11}$$

where D is the perpendicular diffusion coefficient [*Dwyer*, 2010] and R_0 is the initial avalanche radius. The runaway electrons will be spread radially according to a probability distribution, so we chose one e-folding length from the center to define R_D. In doing so, we find the coefficient β to be approximately 1/4 through fitting of Monte Carlo simulation results.

The differential equations governing $R_D(t)$ [*Qin et al.*, 2011] and $\xi(t)$ can be written as:

$$\frac{dR_D(t)}{dt} = \frac{\beta D(E(z(t)))}{2} \cdot \frac{1}{R_D(t)} \tag{2.12}$$

$$\frac{d\xi(t)}{dt} = \left[\frac{\lambda(E(z(t)))}{v_{RREA}}\right]^{-1} \tag{2.13}$$

with $R_D(t=0) = R_0$ and $\xi(t=0) = 0$. Using the Euler method, we can therefore calculate $n_p(z,t) \simeq n_e(z(t))$ by advancing $R_D^{k+1} = R_D^k + \Delta R_D = R_D^k + \beta\frac{D}{2} \cdot \frac{1}{R_D^k}\Delta t$ and $\xi^{k+1} = \xi^k + [\lambda/v_{RREA}]^{-1}\Delta t$, where k is an index representing the time iteration, and Δt is the time step of the simulation.

Rather than looking at a single avalanche as above, we need to take continuous injection of RREA electrons into account. The quantities ξ and R_D then become dependent on both z and t, as they both depend on the history of the electric field along $z(t)$. The density n_p is driven by the following source term:

$$S_{RREA} = \frac{\Delta n_p(z,t)}{\Delta t} = I\left(t - \frac{z}{v_{RREA}}\right) e^{\xi(z,t)} \cdot \frac{\alpha}{\pi \cdot R_D^2(z,t)} \tag{2.14}$$

where seed electrons are added over time at the location $z = 0$, according to the injection function $I(t)$. Throughout this thesis, we use a Gaussian injection function, given by $I(t) = a \cdot e^{-(t-t_\mu)^2/t_{inj}^2}$, where the duration of the injection, t_{inj}, is a free parameter. Because there is no factor of 1/2 in the exponent, $t_{inj} = \sqrt{2} \cdot \sigma$. An injection time of 15 μs therefore corresponds to a standard deviation σ of 10.6 μs. The mean time, t_μ is set as $3 \cdot t_{inj}$. The normalization factor, a, is set so that the function corresponds to a chosen number of initial electrons. Figure 2.3 shows how the information is propagated through time, t, and space, z. As the RREA moves at the speed $v_{RREA} = 0.89c$, the time the RREA uses to cross a simulation grid cell of size Δz is $\delta t = \frac{\Delta z}{v_{RREA}} = \frac{\Delta z}{0.89c}$. For all grid node locations z_j, R_D, and ξ are transported as:

$$R_{D_j}^{k+1} = R_{D_{j-1}}^k + \frac{\beta D_{j-1}^k}{2 \cdot R_{D_{j-1}}^k} \cdot \delta t \tag{2.15}$$

$$\xi_j^{k+1} = \xi_{j-1}^k + \frac{v_{RREA}}{\lambda_{j-1}^k} \cdot \delta t \tag{2.16}$$

where the diffusion radius R_D, the diffusion coefficient D, the exponential term ξ, and the runaway avalanche characteristic length λ, each depend on their values at previous time steps, along their path of propagation.

The multifluid plasma modeling based on equations (2.5) – (2.8) makes use of a variable time step Δt. This time step is based on the electrodynamic state of the system, which is governed by low-energy electrons (see e.g., *Bourdon et al.* [2007]). We emphasize that in the modified model used in the present work, we also determine Δt on the basis of the electrodynamics of the system, while the RREA parameters R_D and ξ (equations (2.15) and (2.16)) evolve through the use of a longer time step δt, which is based on the grid size Δz (see above). In practice, equation (2.15) sets a lower limit on the initial RREA radius chosen, which must be significantly greater than $\sqrt{\frac{\beta D \Delta z}{2 v_{RREA}}}$. For a typical $\Delta z \simeq 1$ m, this implies $R_D \geq 10$ m.

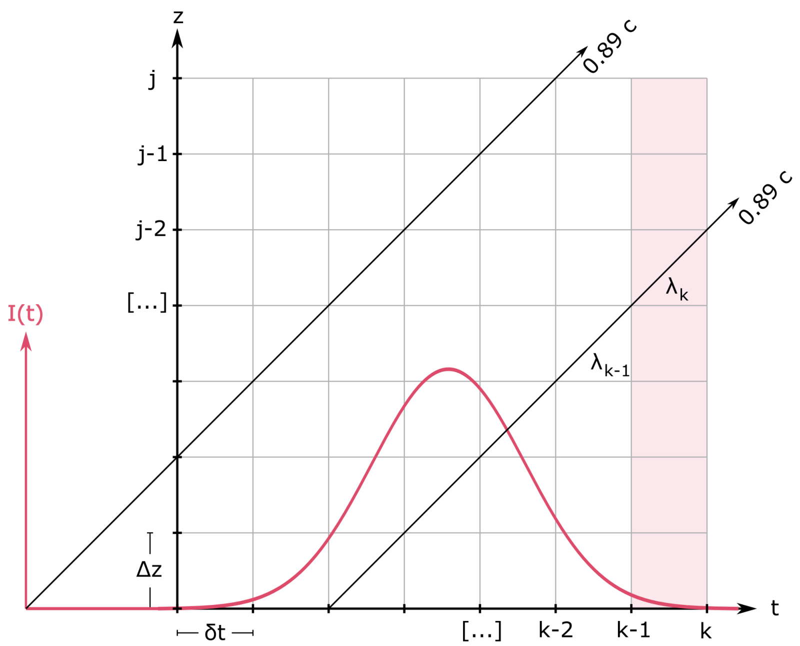

Fig. 2.3: Schematic representation of the propagation of information in the model. Seed electrons are injected according to an injection function, $I(t)$ (red). For each time step, δt, corresponding to the time it takes the RREA to move across one simulation grid size, Δz, new values for the diffusion radius, R_D, and exponential term, ξ, are calculated. The variables are dependent on their previous values, and as such at the current time of the simulation (shaded light red), each grid cell uses information from where the corresponding electrons were at previous iterations (following the diagonal lines).

2.2.2 Radio emission and propagation

Analytical formulation

We propagate the radio signal using the analytical formulation from *Uman et al.* [1975]. The source of the electric current, $i(D,t)$, is modeled as a vertical antenna placed a certain ground distance D and altitude H away from the receiver (see Figure 2.4) above a perfectly conducting ground plane. The magnetic field can then be calculated using:

$$B\phi(D,t) = \frac{\mu_0}{2\pi}\left[\int_0^H \frac{\sin\theta}{R^2} i(z, t - R/c)dz + \int_0^H \frac{\sin\theta}{cR}\frac{\partial i(z, t - R/c)}{\partial t}dz\right] \tag{2.17}$$

where R is the distance from the altitude element dz to the receiver (see Figure 2.4). The effects of ground attenuation at different distances are estimated by applying first-order Butterworth filters and a scaling factor, depending on the distance. A block diagram of the filters used can be seen in Figure 2.6. These filters have been designed to approximate empirical values for ground attenuation over land [*Radiocommunication Sector of ITU*, 2007].

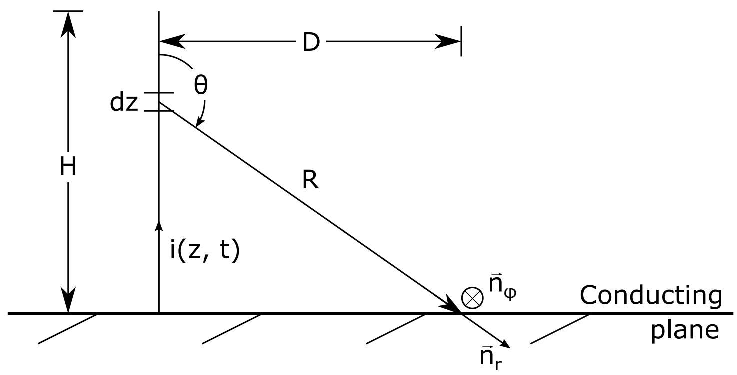

Fig. 2.4: Sketch of the geometry of the antenna above a perfectly conducting ground, whose emission is described by equation (2.17). Based on Figure 2 in *Uman et al.* [1975].

Comparison with an FDTD model

To validate our approach of using *Uman et al.* [1975]'s analytical formulation for the propagation of the radio signal from our simulated current (see Section 2.2.2), we have compared our results with a model based on the Finite-Difference Time-Domain (FDTD) method. A detailed description of the FDTD model can be found in *Marshall* [2012] and *Marshall et al.* [2015]. An FDTD model is much more comprehensive than the simple analytical solution we use, taking the ground, atmosphere, and ionosphere into account. It is consequently much more computationally demanding, which is why we here only use it as a validation for the analytical approach, rather than using the FDTD model throughout the chapter.

In Figure 2.5, we present the result of the model comparison. The current generated by the fluid model presented in Section 2.2.1 has here been approximated by a Gaussian fit of the current in time and space, given by $I = -I_0 \cdot e^{-(z-z_\mu)^2/z_\sigma^2} \cdot e^{-(t-t_\mu)^2/t_\sigma^2}$, where $I_0 = 74.2$ kA, $z_\mu = 12$ km, $z_\sigma = 695$ m, $t_\mu = 54$ μs, and $t_\sigma = 15$ μs. Doing this does not change the analytically propagated signal significantly, but eases the input into the FDTD model.

The FDTD model is here using a ground attenuation based on the signal moving over seawater. The analytical result is presented in two versions — one with no ground attenuation (i.e., perfectly conducting ground), and one with filters approximating propagation over land. As then expected, the FDTD result falls between the two analytical cases (Figure 2.5), demonstrating the validity of our approach.

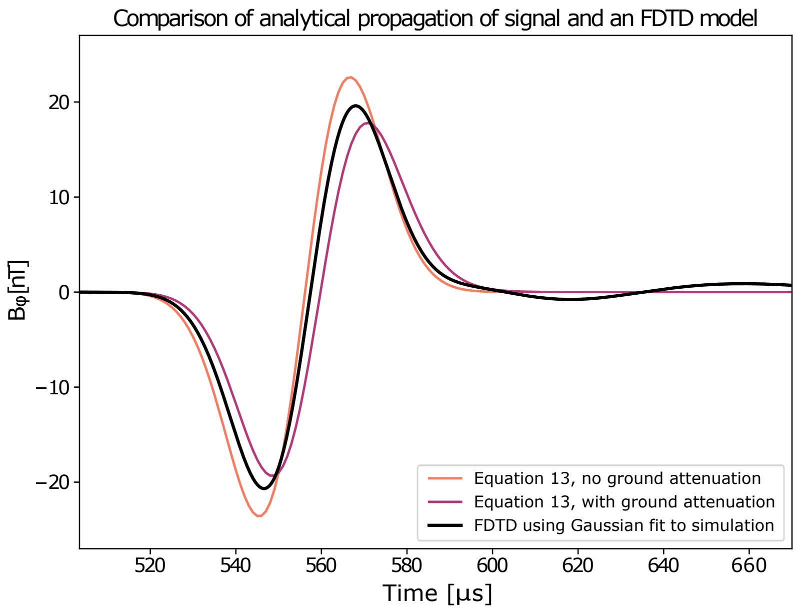

Fig. 2.5: Comparison of a Gaussian fit of our simulated current propagated using an FDTD model (black), and the analytical method outlined in Section 2.2.2 (orange and purple). The orange line represents a case with no ground attenuation applied (conducting ground), while the purple line corresponds to ground attenuation based on propagation over land. The FDTD model is using ground attenuation based on propagation over seawater, which, being more conductive than land, makes the result fall between the two analytical cases.

2.2.3 Slow LF pulse data and detector response

In the study presented in Chapter 3, we compare simulated radio emissions to data of three slow low frequency (LF) pulses occurring simultaneously with TGFs. The slow LF pulses were collected from an orthogonal pair of LF magnetic field coils placed at the Florida Institute of Technology (FT) in the United States. The sensor has an operating bandwidth of approximately 1-300 kHz [*Cummer et al.*, 2011]. To compare simulation results with events observed by this sensor, we apply a series of Butterworth and Chebyshev filters specifically designed to match the detector response, see Figure 2.6. A graph of the sensor frequency response can be found in *Dwyer and Cummer* [2013].

The three slow LF pulses we use were observed on August 3rd 2010, August 10th 2014, and September 4th 2015. They are sometimes refered to by their observation dates as 20100803, 20140810, and 20150904 through Chapter 3. For an in-depth discussion of the events, see *Pu et al.* [2019].

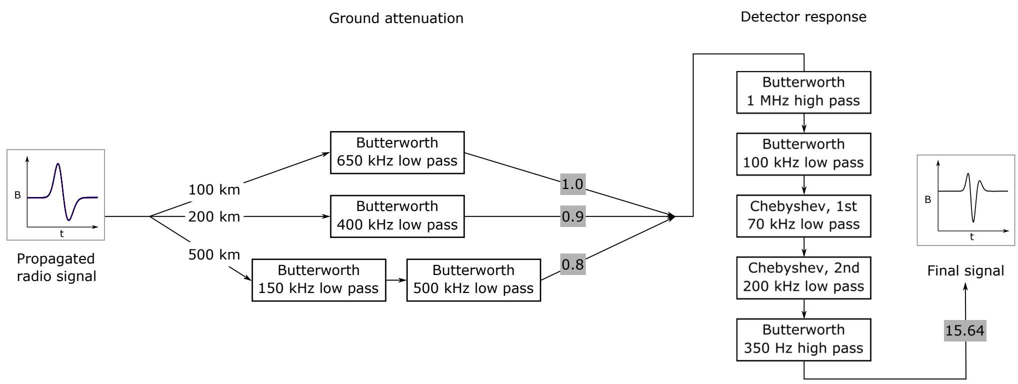

Fig. 2.6: A diagram representing the filters applied to our simulation results to approximate ground attenuation (first group of filters, left), and to mimic the detector response of the LF sensor at FT (second group of filters, right). The small grey boxes represent scaling factors applied to the signal. All Butterworth filters are first order, while the Chebyshev filters have the order noted. For ground attenuation at distances not mentioned here, the distance is rounded to the closest of these three values for the purpose of ground attenuation application only.

2.2.4 Model flowchart

Figure 2.7 gives a schematic overview of the flow of information during the simulations. A source term for electron injection is used as input to the multifluid plasma model (see Section 2.2.1), which gives the current from the moving charged species as an output. This current is then the source of the magnetic field propagated using the analytical formulation in Section 2.2.2, giving the radio emission at a chosen distance. Filters that mimic the ground attenuation and the response of the antennas with which we compare results are then applied in order to obtain the final signal.

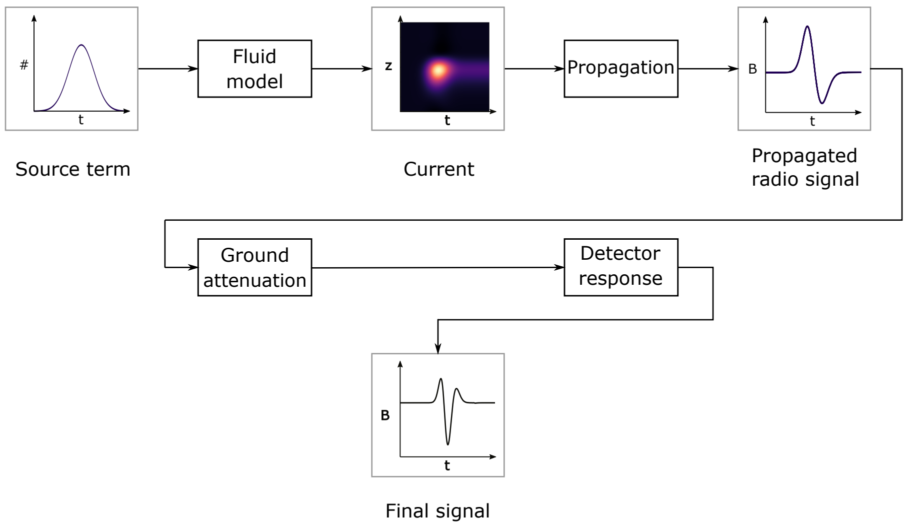

Fig. 2.7: Schematic representation of the information flow during modeling. The black rectangles represent steps of the modeling process. The input into the next step is the output from the previous, shown in grey squares. This figure provides a general overview, for details concerning the ground attenuation and detector response, see Figure 2.6.

Chapter 3

Modeling Low-Frequency Radio Emissions from TGF Sources

In this chapter, we use the methods presented in Section 2.2 to model LF radio emissions from the currents generated by RREAs at a TGF's source. The background for this study was introduced in Section 1.3.

3.1 LF emissions from the TGF source region

The following results were obtained using a simulation domain of 6 km length and 2 km radius. In this case, $2 \cdot 10^{15}$ electrons are injected into an electric field corresponding to 3.57 kV/cm (or 1.27 RREA thresholds) at ground level, scaled to 12 km altitude. The validity of these assumptions will be discussed in Section 3.2. The initial field extends over the first two thirds of the 6 km domain to avoid interference from the simulation boundary. The background field is initially set as zero in the last third, so as to ensure the dampening of the RREAs before they reach the end of the simulation domain. The electrons are injected following a Gaussian distribution in time with the duration of the injection being $t_{inj} = 15$ μs, corresponding to a standard deviation of 10.6 μs.

Figure 3.1 shows a map of the total current obtained using these initial conditions. The total current is obtained through integration of the current flux over cross-sections of the simulation domain. The total current flux is the sum of positive and negative ions, electrons, and the displacement current. The z-axis shows the current along the length of the simulation domain. The abscissa shows the development in time. The duration of injection of 15 μs determines the rise time of the current, which peaks at 74.2 kA. The decay of the current is primarily driven by three-body attachment. The remaining tail of current is due to ion drift in the electric field, and falls off slowly over a timescale of several milliseconds. In 3 ms, the tail reduces to 60% of of its amplitude right after the initial peak.

Figure 3.2 shows the resulting radio signal as it would be registered by the detectors used by *Pu et al.* [2019]. The signal has been propagated over a ground distance of 156 km from the source using the analytical formulation described in Section 2.2.2. Filters have then been applied to approximate the filter response (Section 2.2.3). The result is compared with data collected at the FT, on the 4th of September 2015 [*Pu et al.*, 2019].

As can be seen, the simulation result and the slow LF pulse are similar in shape, amplitude, and duration. The asymmetry of the first and second positive peaks is present in both cases, with a ratio of the first to second positive peak being 1.63 for the slow LF pulse and 1.70 in the simulation.

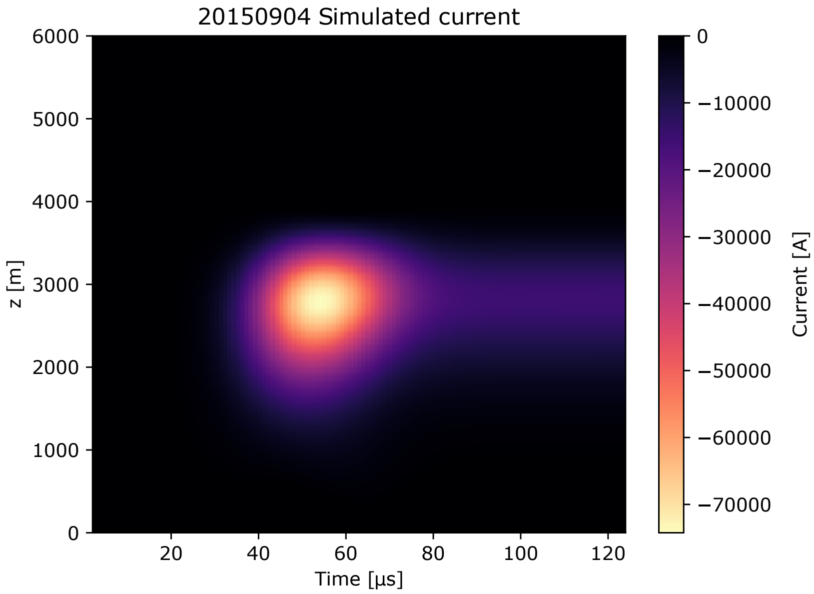

Fig. 3.1: Map of the current produced by our simulation along the z-axis, and its evolution in time.

The difference in amplitude between the positive and negative peaks is a bit larger — the ratio between the first positive peak and the negative peak is -0.74 for the slow LF pulse, and -0.58 for the simulation. The duration of the slow LF pulse is given by *Pu et al.* [2019] as 65 μs. The duration of the current obtained by our simulation is similar; $\pm 2 \cdot t_{inj}$ is 60 μs. Our simulation results have a slightly slower decrease towards the end of the signal than the slow LF pulse. The injection time of the seed electrons is a free parameter in our simulations, and has as such been chosen to fit the slow LF pulse as closely as possible.

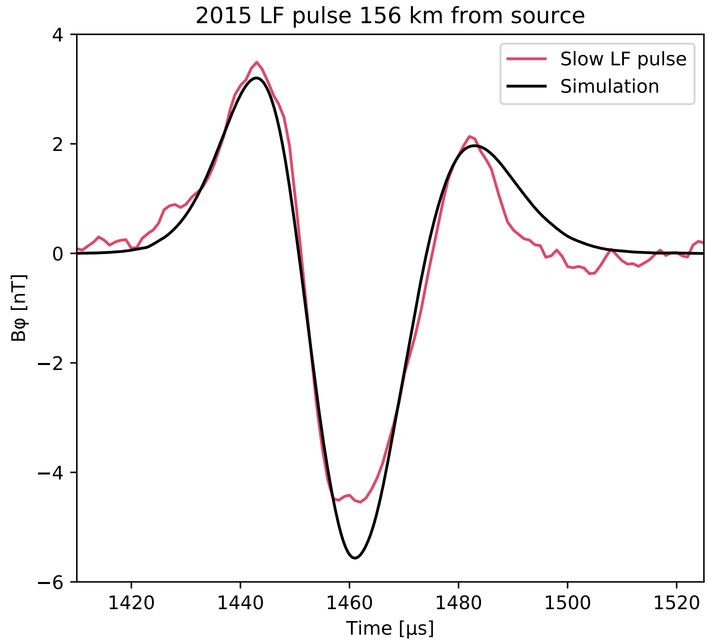

Fig. 3.2: Simulation results compared to a slow LF pulse. The LF pulse was detected 156 km from the source, and the simulated radio emission has been propagated the same distance. The curves have been aligned in time.

3.2 Results and discussion

3.2.1 Validity of initial conditions

The physical context of the simulations performed in this chapter is that of a lightning leader injecting seed runaway electrons into a large-scale, homogeneous electric field. The number of seed electrons used varies around 10^{15}, which is on the lower side, but consistent with previous papers using such a context [e.g., *Celestin et al.*, 2015; *Mailyan et al.*, 2019]. The electric fields we use are, with small variations, around 1.3 times the threshold RREA field [*Dwyer et al.*, 2012]. Since no RREAs will happen below the threshold field, this is then a relatively low field as RREA-related processes go. We assume the air density of 12 km altitude, and this is also where we place the peak of the current when propagating its radio signal. This is consitent with previous literature on TGFs [e.g., *Cummer et al.*, 2014], and it is also within the range of source altitudes for the slow LF pulses as described in *Pu et al.* [2019].

Finally, using these initial conditions, we find the number of runaway electrons at the midpoint of our simulation domain to be in the $10^{17} - 10^{18}$ range (see Table 3.2.2), which is consistent with the number of runaway electrons necessary for TGF production [e.g., *Østgaard et al.*, 2012].

3.2.2 Comparison to other observations

In Figure 3.3, the result presented in Section 3.1 is compared to two other detections of slow LF pulses from FT. While the first observation was done 156 km from the source, these two are significantly farther away. One was done on August 3rd 2010, at a distance of 466 km from the source, and the other on August 10th 2014, 472 km from the source. Our simulation result is clearly a poorer match for these events, noticeably the amplitude of the signal is significantly too low. This implies that the different observations presented in *Pu et al.* [2019] are inherently different — these two events correspond to a stronger source signal than the event seen in the previous section. We conclude that there must be a range of initial physical conditions capable of creating slow LF pulses.

Examples of better fits for these two events can be seen in Figure 3.4. Case (a) is the observation from 2010, which was 466 km away from the source. Case (b) is from 2014, at 472 km distance. The initial parameters of the

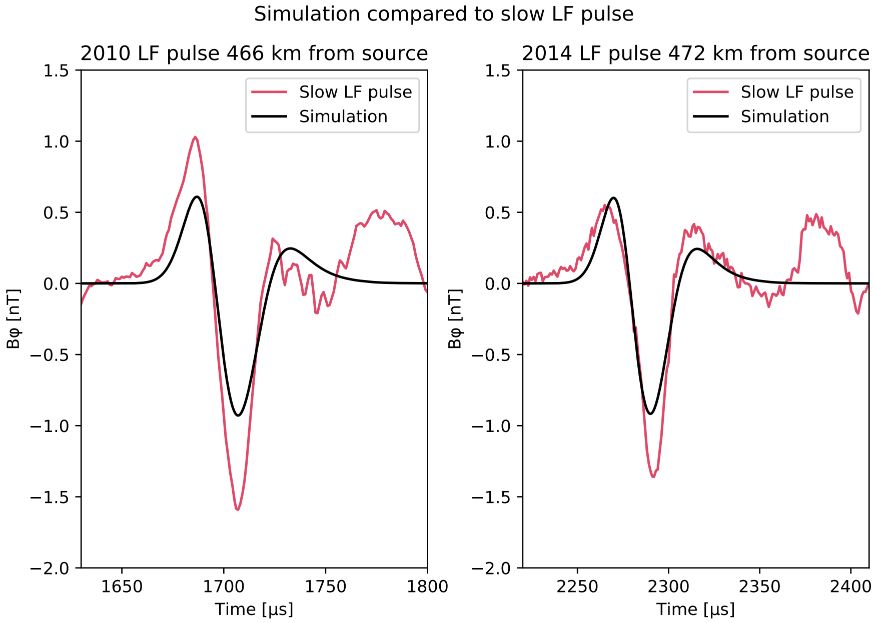

Fig. 3.3: The same simulation as shown in Figure 3.2, here propagated to 466 km (left) and 472 km (right) to match detections done at FT on 3 August 2010 and 10 August 2014, respectively. In the observational data (red) one can see the ionospheric reflection of the signal following the slow LF pulse, which is not included when using our analytical approach to radio propagation.

simulations for these cases are summarized in Table 3.2.2. The simulation presented in Section 3.1 is also included for comparison. The simulation domain length and radius remain 6 km and 2 km, respectively, through all the cases. The external electric field extends for the first 2/3 of the length throughout. The peak current and the number of runaway electrons at the mid-point of the simulation are included in Table 3.2.2. The peaks following the slow pulses here are due to ionospheric reflection of the signal. These results are not necessarily unique, i.e., there might be other configurations of initial parameters that give equally good matches. The following section will describe the impact of varying the free parameters in our model.

	20100803	**20140810**	**20150904**
Distance from source [km]	466	472	156
Initial parameters			
Electric field [kV/cm]*	$3.77 \cdot 10^5$	$3.57 \cdot 10^5$	$3.57 \cdot 10^5$
Duration of injection [μs]	15	15	15
Initial number of electrons	$9 \cdot 10^{14}$	$3 \cdot 10^{15}$	$2 \cdot 10^{15}$
Results			
Maximum current [kA]	117.50	94.38	74.24
Runaway electrons**	$1.75 \cdot 10^{18}$	$9.00 \cdot 10^{17}$	$7.10 \cdot 10^{17}$

Table 3.1: Table of initial parameters, as well as some selected results, for the three events. *The table value is the electric field scaled to ground-level. The simulation is performed at 12 km altitude, which is consistent with a source altitude of 10 – 15 km found by *Pu et al.* [2019]. **Corresponds to the number of runaway electrons in the mid-plane of the simulation domain.

3.2.3 Contributions of different initial parameters

Different initial conditions of the simulation will naturally yield different results. The free parameters we have in the current model include the duration of injection, the number of initial seed electrons, the amplitude of the external electric field, the extent of the electric field, and the radius of injection.

The time-profile of electron injection follows a Gaussian function throughout the chapter. Interestingly, we find that moderate changes of the initial RREA radius produce negligible changes in the final result. The injection time has been chosen to fit the observations we have access to. Changing it changes both the shape and amplitude of the result, as well as of course its duration. Changing the initial number of electrons and the initial electric field will also affect the results' shape and amplitude. In general more electrons, a stronger field, and a larger extent of the field will all lead to a stronger resulting pulse. This also means that decreasing some and increasing others of these values to some degree can balance each other out, creating a range of values that can give reasonable results. Since the parameters all affect each other, the number of possible combinations quickly becomes large, and we have not performed a full analysis of the whole parameter space. Our model also has numerical limitations. In particular, when the initial conditions lead to very high particle densities, the time step of the simulation becomes too small to get results within any reasonable time frame.

To give the reader a feel for how changing the initial parameters may change the results, we present some examples in Figure 3.5. We have here kept the case presented in Section 3.1 as a reference, and varied one parameter at a time. As can be seen, even small changes in the initial parameters produce visible changes of both the shape and amplitude of the signal. Increasing the injection time increases the duration of the signal as expected, and also diminishes the amplitude. Increasing the electric field, number of seed electrons, and the length of the simulation domain (and thereby the extent of the electric field, which is still 2/3 of the domain length) all cause an increase of the amplitude of the signal, albeit in subtly different ways. The shape of the signal, that is, the ratios between the different peaks, changes in different ways for the different parameters. The peak current and resulting number of runaway electrons also differs. A summary of these properties of the results can be seen in Table 3.2.

The variations shown in Table 3.2 and Figure 3.5 are small, and cannot be considered physically less reasonable choices for initial parameters than those of the reference case from Section 3.1. Combined with the inherent difference of the three observations of slow LF pulses presented in Sections 3.1 and 3.2.2, this suggests that a range of physical conditions can and do produce LF pulses with recognizable characteristics. While all the parameters presented cause a change in the final signal, future refinement of the simulations and larger data sets of slow LF pulses may allow for further constraints on the physical conditions necessary for slow LF pulse production.

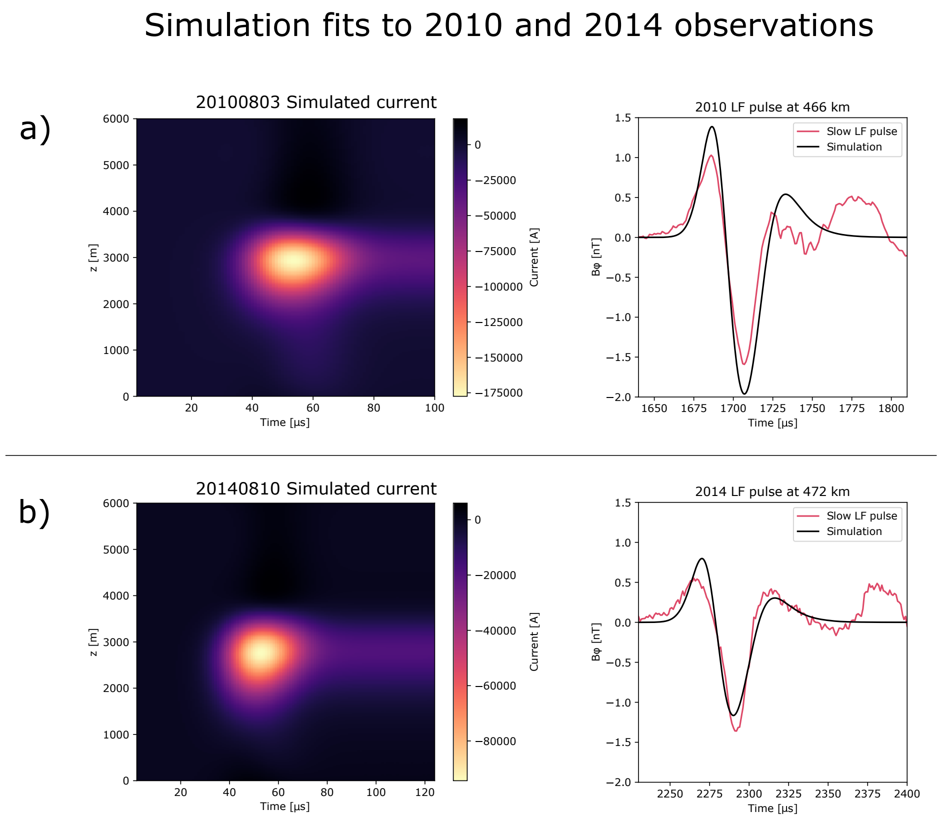

Fig. 3.4: Simulations of the current created by the RREA (left), and the resulting radio pulse (right). The initial parameters of the simulation are made so that the radio pulse (black, right) fits the observations (red, right) from 3 August 2010 (a) and 10 August 2014 (b). See text for description of the parameters. In the observational data, one can see the ionospheric reflection of the signal following the slow LF pulse.

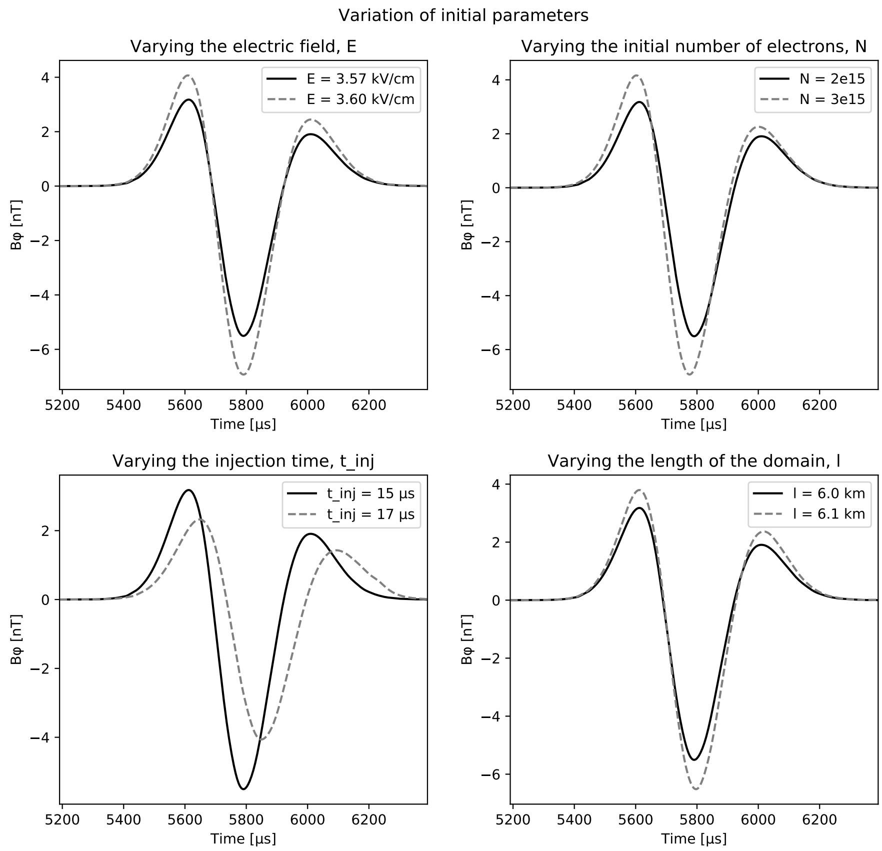

Fig. 3.5: Variation of different initial parameters of the simulation. The black line in all four subplots is the case presented in Section 3.1. The grey dashed lines each represent a variation of this case, where the value of one parameter has been changed slightly, while all the others have been kept the same as the case in black. That is, in the first subplot only the electric field has been changed, not the parameters presented in the other subplots.

	Reference	E = **3.60 kV/cm**	$N = 3 \cdot 10^{15}$	t_{inj} = **17 μs**	l = **6.1 km**
Peak current [kA]	74.24	93.07	93.38	66.68	86.63
Number of runaway electrons	$7.10 \cdot 10^{17}$	$9.00 \cdot 10^{17}$	$9.01 \cdot 10^{17}$	$7.12 \cdot 10^{17}$	$8.35 \cdot 10^{17}$
Ratio of positive peaks	1.70	1.66	1.84	1.71	1.60
Ratio of first peak to negative peak	-0.58	-0.59	-0.60	-0.58	-0.58

Table 3.2: Table of selected results while varying the initial parameters one by one, compared to the reference case presented in Section 3.1. These are numerical values for the results presented in Figure 3.5. The first column contains the values of the reference case (the solid black curve in Figure 3.5), while the four following columns correspond to the variations presented in dashed grey lines in the four subplots of Figure 3.5.

3.3 Conclusions

1. Using a multifluid plasma model, we find that TGF producing RREAs should be naturally associated with the emission of slow LF pulses.

2. The timescale of the final signal is dependent on the timescale of the initial electron injection. Using an injection time of 15 μs, we get a final signal of similar duration as observations of slow LF pulses.

3. The magnitude of the electric field, the length of the simulation domain, the injection time of seed electrons, and the initial number of electrons all change the shape and amplitude of the signal. This constrains the combinations of parameters which yield results in agreement with observational data.

4. The cases we have presented all use initial parameters that are in physical agreement with the scenario of a leader injecting runaway electrons over a region of space, followed by a RREA. This means this scenario is compatible with current observations of TGF-associated slow LF pulses.

Chapter 4

Downward-directed Terrestrial Gamma-ray Flashes

This chapter is based on a paper published in the journal Geophysical Research Letters by *Berge and Celestin* [2019]. The Monte Carlo model used for photon propagation was presented in Section 2.1. An introduction to this work and ground observations of TGFs in general can be found in Section 1.4.

4.1 Time dispersion

Figure 4.1a shows the impulse response of an instantaneously produced TGF on ground and at satellite altitude at radial distance 1166 m and 200 km, respectively. Ninety percent of the photons from a simulated downward-directed TGF impulse with source at 3 km altitude reach ground in about 1.5 μs. For an upward TGF impulse originating at 12 km, it spreads over

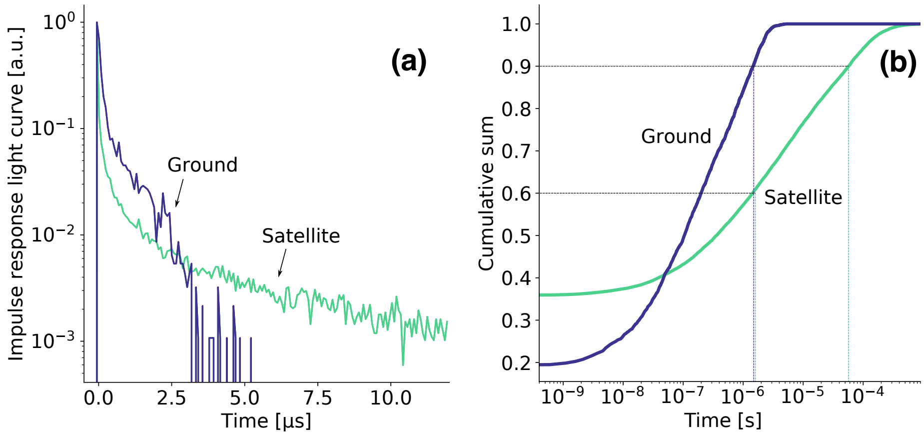

Fig. 4.1: a) Impulse response of an instantaneous TGF at satellite altitude (green) and ground (blue). Both lines are normalized to peak at 1, to best compare the shape of the light curve. b) Normalized cumulative sum of photons from an instantaneous TGF arriving at satellite altitude (green) and ground (blue). The points where 60 % and 90 % of photons have arrived are marked with dashed lines.

more than 57 μs. This shows that time dispersion due to scattering of the gamma rays is smaller on the ground than at satellite altitude. We have verified that this is due to shorter distances traveled, not to the number of times each photon is scattered. However, the majority of photons at satellite altitude arrive within a very short time. As an example, the first 60% arrive within 1.6 μs (see Figure 4.1b). The long duration to reach 90% is due to a minority of photons. *Abbasi et al.* [2018] observed time structures of less than 10 μs over a few hundred microseconds. Since the duration of the impulse response is only a few microseconds, we conclude that such structures should be observable at satellite altitude given sufficient time resolution, if they are present in upward TGFs.

Space-based detectors have observed some TGFs to be pulsed. While the duration between pulses is generally in the order of milliseconds [*Fishman et al.*, 1994; *Marisaldi et al.*, 2014; *Mezentsev et al.*, 2016], overlapping pulses with sub-millisecond separation also occur [*Briggs et al.*, 2010; *Foley et al.*, 2014; *Stanbro et al.*, 2018]. It remains an open question whether this is due to different production mechanisms for the events of *Abbasi et al.* [2017, 2018] and TGFs detected from space, or whether such time structures always exist, but are not observable. The latter case could be due to detector limitations.

4.2 Geometry

Figure 4.2 shows simulation results illustrating how an idealized TASD observation could look for a TGF with a tilt of 30° and a beam width of 20°. It is reminiscent of the detections reported in *Abbasi et al.* [2017], where the events observed by the TASD also tend to register in more than 10 detectors, see Figure 1.4 for comparison. This simulation shows the difficulty of accurately inferring the original geometry from such detections. The black cross shows where the middle of the projected beam would have hit in vacuum, and the grey ellipse marks the footprint of the projected beam. The red cross marks the mean as calculated from the hits in the detectors. We can see how the mean is shifted towards the TGF source, here set at origin, as the photons had to traverse less atmosphere on this side of the beam. A similar effect was found in *Celestin et al.* [2020]. The observed footprint is also significantly blurred.

To quantify how results of this kind can be used to determine the geometry of

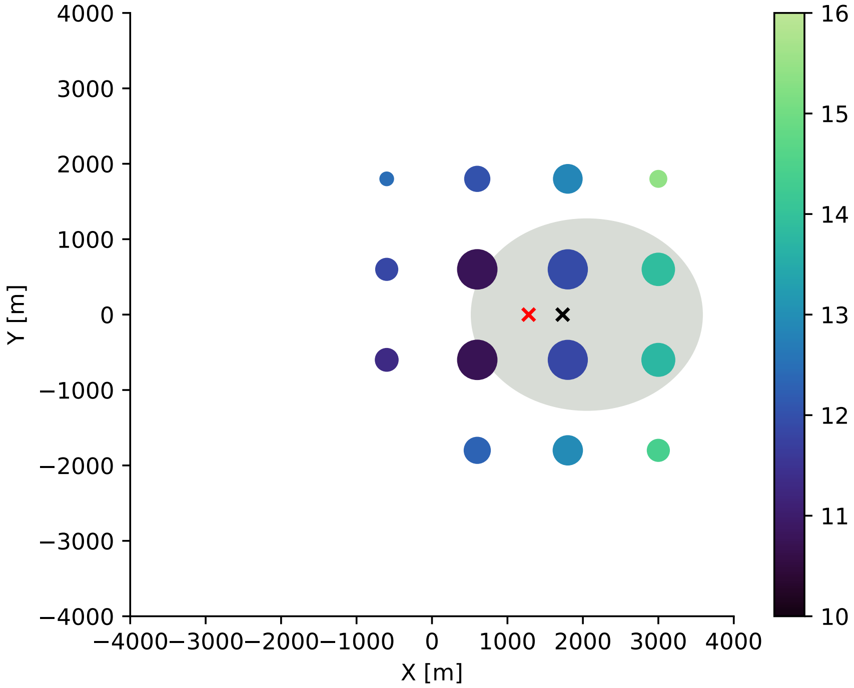

Fig. 4.2: A simulated TGF initiated at origin and 3 km altitude with a beam width of 20° and a tilt of 30°, as it would be detected by an ideal detector set-up similar to that of *Abbasi et al.* [2017, 2018], see Figure 1.4 for comparison. Each point represents one detector. The point size corresponds to the logarithm of the number of photons hitting each detector, while the color corresponds to the median time of arrival in microseconds. The black cross shows where the middle of the projected beam would have hit in vacuum, the ellipse marks the footprint of the beam without atmospheric effects. The red cross marks the mean as calculated from the hits in the detectors.

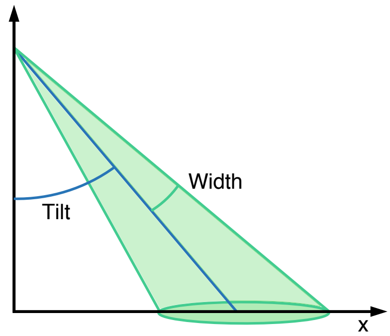

Fig. 4.3: Configuration of the initial beam geometry. The beam width is varied from 10° to 45°, and the beam is tilted between 0° and 35°.

the initial beam, we have analyzed a series of simulations with different initial conditions. The beam width was varied from 10° to 45°, and the beam was tilted between 0° and 35° (see Figure 4.3 for an illustration of the geometry). We define the axis of the tilt, meaning the line between the footpoint of the TGF's initial position and the mean position of the photons that reached ground, as the x-direction. These metrics can be applied to real detections, as the source position can be determined using a lightning mapping array *Abbasi et al.* [2018], and the mean position is a relatively accurate measure even with discrete detectors.

Saving the positions of all photons that reached ground in the different configurations, we created a parameter space of the mean and standard deviation of the photons' position along the tilt axis, x. The results can be seen in Figure 4.4, where each point represents a different initial configuration. Most configurations have a uniquely defined position in this parameter space, indicating that the initial geometry can be found. However, a few initial configurations yield similar results and make identification difficult. This concerns combinations of larger tilts ($\geq 20°$) and very wide beams ($> 40°$). The error bars

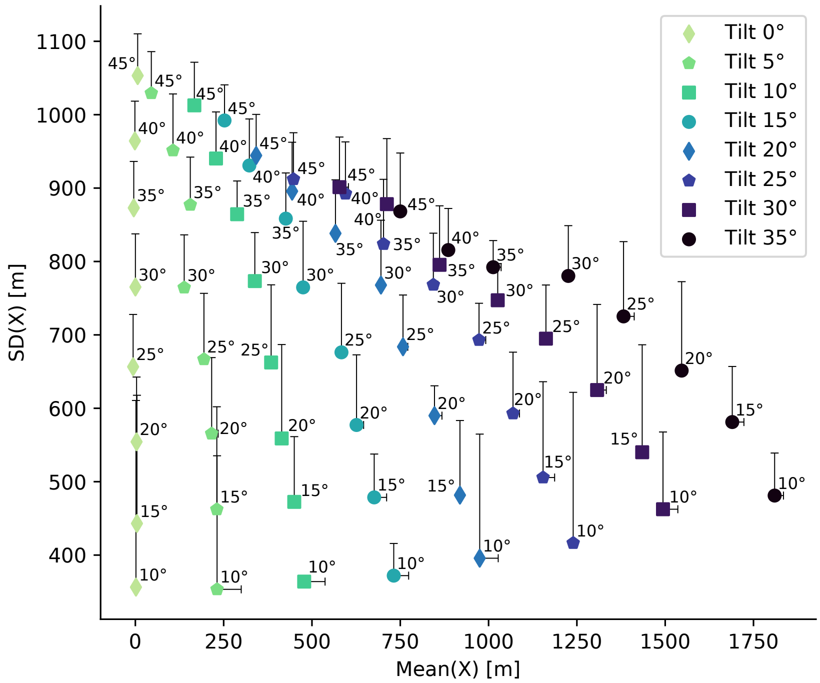

Fig. 4.4: Parameter space with mean position along the x-axis versus standard deviation of position along x. The x-axis is defined as the line between the source and the mean position of detections. Each point on the plot represents one simulation with given initial conditions. The color and shape vary with the tilt angle, while the beam width is printed next to each point. The error bars describe the difference we get if the numbers are calculated from discrete ideal detectors representative of those used by *Abbasi et al.* [2017, 2018], rather than from each photon's exact position.

signify the difference in mean and standard deviation obtained from calculating the values from discrete detectors representative of those used by *Abbasi et al.* [2017, 2018] (as in Figure 4.2), rather than using the exact positional values from our simulations. The difference of the mean values is very small, while for the standard deviation the change is larger. The calculated standard deviation will increase with the distance between detectors. The points of the parameter space remain resolved, just shifted upwards, for most configurations, especially around the middle of the angular ranges used. This remains the case when the beam is aligned differently with respect to the detector grid. Through simulations, one can calibrate the expected increase in standard deviation to specific detector grids.

To further distinguish detections where this parameter space is inconclusive, one can consider the asymmetry of the detection, i.e., how many detections fall below the mean position compared to above. The asymmetry generally increases with both tilt and beam width, but is sensitive to the alignment of the beam with the detector grid. Such considerations would therefore have to be made with simulations on a case-to-case basis.

4.3 Energy spectra

The initial energy spectrum of a TGF depends on its exact production mechanism. We use initial spectra corresponding to runaway electrons produced in inhomogeneous fields at leader tips with potential drops from 60 to 300 MV [*Celestin et al.*, 2015], as well as an exponential spectrum with cutoff at 7.3 MeV as produced by a full RREA developing in a large-scale electric field [*Coleman and Dwyer*, 2006]. The different initial spectra can be seen in

Figure 4.5. Different leader potential drops are thought to be associated with different numbers of initial photons, where the harder spectra correspond to a greater number of photons [*Celestin et al.*, 2015], see Table 4.1. TGFs are generally considered to start out with around 10^{18} photons [*Smith et al.*, 2011; *Østgaard et al.*, 2012]. Here we use $2 \cdot 10^{18}$ photons in the RREA case, which is the same number as for the 300 MV potential drop spectrum. We only consider photons with energies greater than 10 keV.

Photons lose energy as they propagate through air. Consequently softer spectra have a lower percentage of the photons reaching ground, as more photons will be absorbed during propagation. Table 4.1 shows the fraction of photons reaching ground for the different initial spectra used. The decrease in number is more severe for softer spectra. The resulting energy spectra on ground with their respective magnitudes can be seen in Figure 4.5b.

It follows that both the shape of the energy spectrum and the number of photons observed on ground depend on the initial spectrum. This should be taken into account when making estimates of the initial conditions corresponding to a ground observation, as the difference between the 60 MV and the RREA case is almost an order of magnitude.

As an example, if one considers the case of the 60 MV potential drop and $6 \cdot 10^{14}$ initial photons, only $\sim 4 \cdot 10^{-5}$ of them reach ground, giving a total of $\sim 2 \cdot 10^{10}$ photons that could be observed. For harder spectra, such as the RREA spectrum, the fraction is much higher — out of one, $\sim 4 \cdot 10^{-4}$ reach ground. If one were to have such an observation and calculate the number of initial photons, but using the rate of photons reaching ground with the RREA spectrum, one would find $\sim 6 \cdot 10^{13}$, an order of magnitude too few. As the initial number of photons associated with softer spectra is presumably lower, this can explain the range of 10^{12} - 10^{14} initial photons obtained by *Abbasi et al.* [2018].

Spectrum	Initial number of photons	Fraction reaching ground
60 MV	$6 \cdot 10^{14}$	$4.0 \cdot 10^{-5}$
160 MV	$4 \cdot 10^{16}$	$1.5 \cdot 10^{-4}$
300 MV	$2 \cdot 10^{18}$	$1.9 \cdot 10^{-4}$
RREA	$2 \cdot 10^{18}$	$3.7 \cdot 10^{-4}$

Table 4.1: Initial number of photons and the simulated fraction of photons reaching ground for the different spectra in Figure 4.5. Initial numbers as function of potential drop are from *Celestin et al.* [2015].

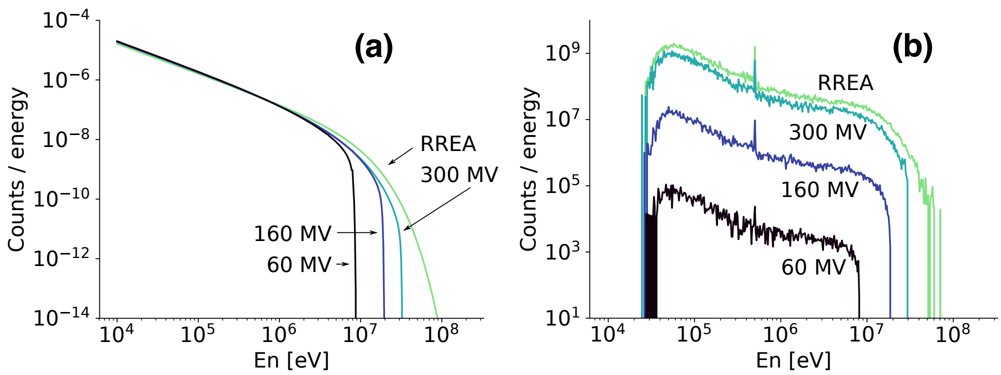

Fig. 4.5: a) Initial photon energy spectra corresponding to leader potential drops from 60 to 300 MV, and an RREA spectrum with cutoff at 7.3 MeV. The spectra's magnitudes are aligned, not accounting for a difference in number of photons. b) Photon energy spectra as they present on ground, corresponding to leader potential drops from 60 to 300 MV, and an exponential RREA spectrum with cutoff at 7.3 MeV.

4.4 Conclusions

The conclusions of this work can be summarized as follows:

1. Despite the differences in distance traveled by the photons, the time dispersion seen in the impulse responses of TGFs measured at satellite altitude and at ground share a steep peak lasting only microseconds. If pulses of duration shorter than 10 μs with tens of microseconds separation occur in the production of TGFs, they should be observable from space, given instrumentation with sufficient time resolution.

2. Most TGF beaming geometries can be uniquely identified by the mean and standard deviation of the detections' position along the tilt axis. Further distinction could be done using a measure of the asymmetry along the tilt axis on a case-to-case basis. This demonstrates the great potential of arrays of evenly spaced ground-based gamma ray detectors, along with lightning mapping, to establish the TGF source position.

3. The number of photons arriving at the ground is heavily dependent on the photons' initial energy spectrum, which may be a source of error when evaluating the number of photons at the source. *Abbasi et al.* [2018] estimate their observations to correspond to $10^{12} - 10^{14}$ initial photons. This could be consistent with a burst of gamma rays produced by lightning leaders forming potential drops of 60 MV.

Chapter 5

Low-energy X-rays from TGFs

Secondary photons – the bremsstrahlung from electrons "knocked free" by a propagating TGF – are a measure of the energy deposited into the atmosphere by a TGF. The background for the work done in this chapter was discussed in Section 1.5, including the definitions of the terms *secondary electrons* and *secondary photons* as they are used here. The results in this chapter were obtained using methods described in Section 2.1.

5.1 Primary and secondary photons

The spectrum of secondary photons depends on the initial spectrum of the TGF, as well as on both the beaming geometry of the TGF, and the position of an observing satellite compared to the TGF. We always assume the TGF to be a point source, beamed isotropically within an opening angle, see Figure

5.1. The radial distance of the observer is measured from the midpoint of the TGF in the xy-plane. When creating energy spectra at satellite altitude, we collect the photons that arrive in a ring of radius $r \pm dr$, see Figure 5.1. Satellite altitude is set to 500 km throughout this chapter.

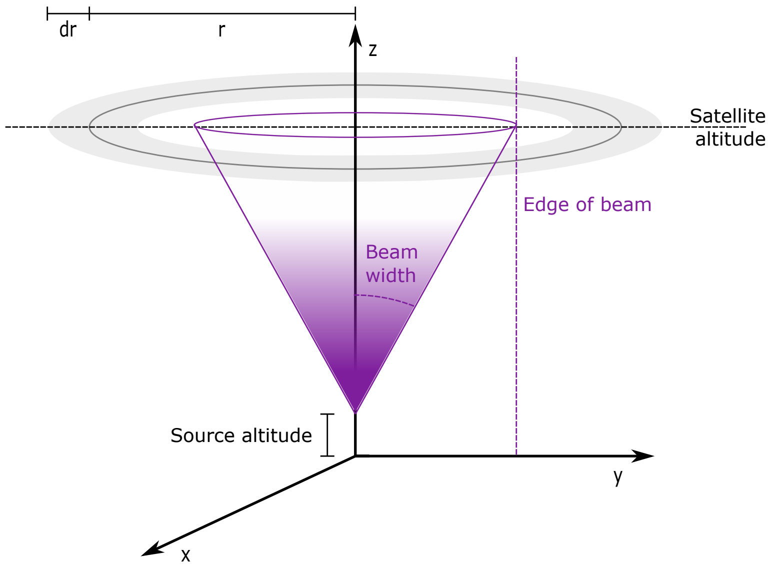

Fig. 5.1: The initial beaming geometry of a TGF with a certain beam width. The photon velocities are distributed isotropically within the purple cone. Photons are collected at satellite altitude within a ring (grey) at a given radius r with a margin $\pm dr$.

An example of a TGF spectrum with the primary and secondary photons separated is shown in Figure 5.2. This case is with a source at 12 km altitude, a beam width of 30°, and the spectrum is collected at a radial distance of 200 ± 50 km. As can be seen, there are significantly fewer secondary than primary photons, bearing the logarithmic scale in mind. In this case, the fraction of secondary to primary photons is 0.17, meaning that a significant part of TGF photons is in fact made up of secondary photons. Presumably, this ratio is not measurable, as the two populations will be mixed as they reach a detector, so that one will only observe the total spectrum.

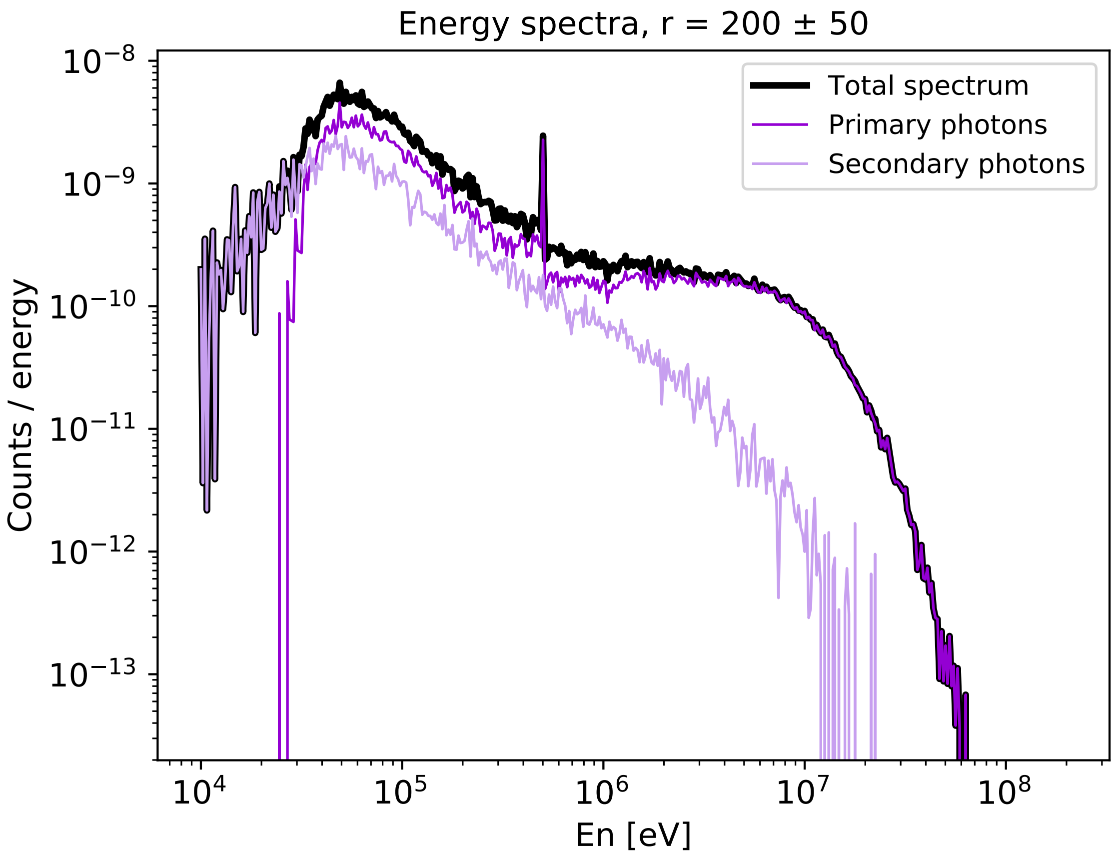

Fig. 5.2: Primary (dark purple) and secondary (lavender) photon spectra for a TGF with a source at 12 km altitude, and a beam width of 30°. The secondary photons make up 17% of the total spectrum.

5.2 Proposed measures

Since the fraction of secondary to primary photons is not measurable over the full spectrum, what remains is the lowest energy portion of the spectrum, which below $\sim$ 30 keV consists exclusively of secondary photons. Here, we will propose some measures that can be applied to the total spectrum in order to extract information from the secondary photons.

The simplest measure is the fraction of low-energy photons to the total number of photons. We use 30.2 keV as the threshold for counting a photon as low energy. The only reason that it is not an even 30 keV is the energy binning we use for the spectra. The low-energy fraction is 0.004 in the example presented in Figure 5.2.

This measure has merit, but also an issue — the shape of the high energy part of the primary photon spectrum varies significantly with the observation geometry. An example can be seen in Figure 5.4, where the high energy "bump" is significantly larger in panel (a1) than in (c1). This means that in some cases the low-energy part may be similarly placed in comparison to the lower range of primary photons, but the total number of primary photons vary, making the low-energy fraction different.

We therefore propose two additional measures, meant to place the low-energy part of the spectrum (which is entirely made up of secondary photons) in regards to the lower-energy part of the primary spectrum (the area $\sim$30 – 150 keV). In order to do this, we fit a line to the $<$ 30 keV part of the spectrum (see Figure 5.3). This is a simple linear fit, done to avoid effects from the relatively high noise level our simulation results have in this part of the spectrum. The next of our proposed measures is simply the slope of this line in a log-log space. This measure tells us how fast the spectrum falls off towards the lowest energies.

For the last measure, we place two points, shown as black dots in Figure 5.3. One is at the peak of the primary spectrum (more precisely, for energies $<$ 511 keV, as the 511-keV peak can exceed the intended peak in some cases). The other point is where the line fit to the low-energy spectrum intersects 25 keV. This energy was chosen to ensure some distance to the lowermost part of the primary spectrum. The last measure is the fraction of the 25-keV point to the peak. This gives an indication of how the low-energy part is placed in comparison to the primary spectrum.

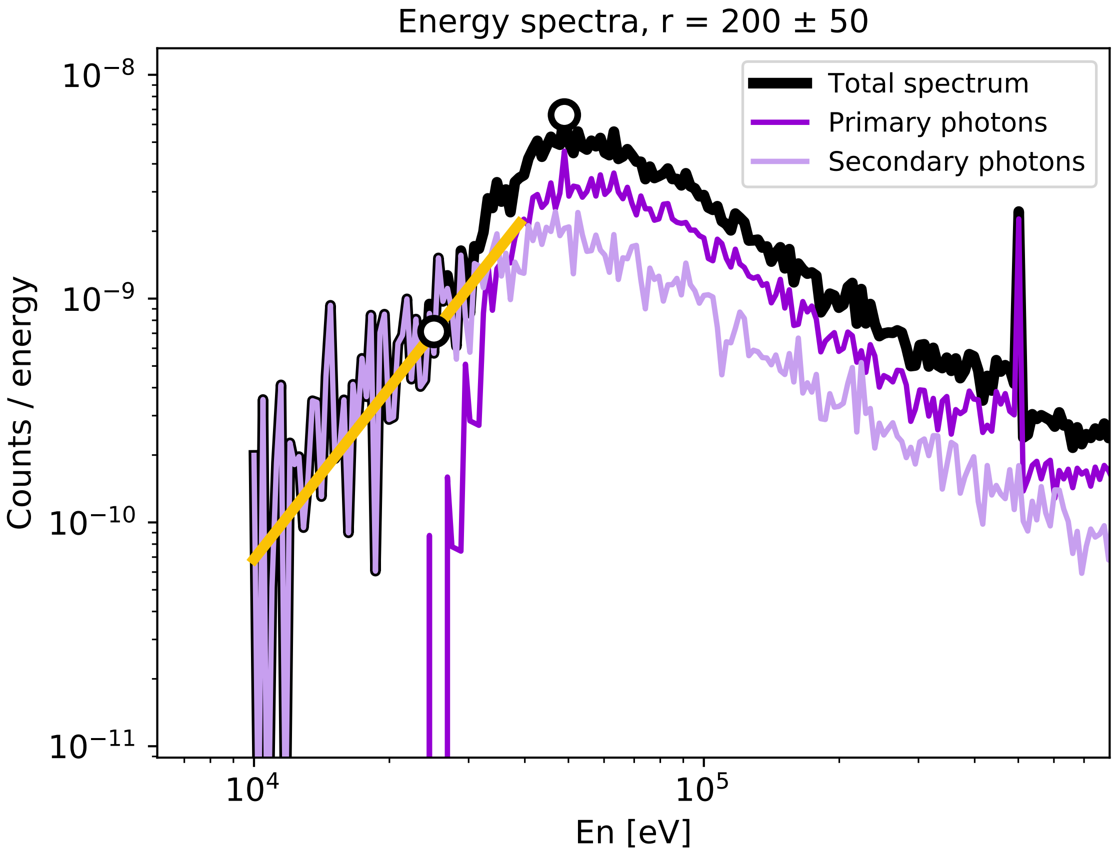

Fig. 5.3: Zoomed in view of Figure 5.2. In addition to the energy spectra, the line fitted to the low-energy part of the spectrum (yellow) and the two black circles mark the points where we make a fraction from the low energy part to the peak are shown.

5.3 Varying initial parameters

In the previous section, we introduced the tools we use to explore how the secondary photons are affected by different TGF configurations. We have chosen to focus on the beam width, production altitude, and energy spectrum, which are described in the following subsections.

5.3.1 Beam width

We have chosen three beam widths; 15°, 30°, and 45°, which span from a quite narrow to a quite wide TGF [e.g., *Gjesteland et al.*, 2011]. For each beam width we present two spectra, one is made from photons in a ring of radius 80 ± 50 km at satellite altitude, and another at radius 550 ± 50 km. See Figure 5.1 for a sketch of the geometry. These radii were chosen as the first falls completely inside the beam for all beam widths, and the other is outside the beam for all. The results can be seen in Figure 5.4.

Beam width	Radius	Low-energy-to-total	Slope	25-keV-to-peak
15°	80 ± 50 km	0.00454	1.34	0.27340
	550 ± 50 km	0.00166	4.27	0.01901
30°	80 ± 50 km	0.00376	2.60	0.11817
	550 ± 50 km	0.00201	5.91	0.01612
45°	80 ± 50 km	0.00326	3.08	0.06984
	550 ± 50 km	0.00198	3.51	0.02637

Table 5.1: Measures of secondary photon spectrum for different initial beaming angles of the TGF.

As can be seen, there is quite a large variation in how the low-energy part of the spectrum is shaped. We see that the slope is significantly steeper for the spectra at 550 km radius (right column of Figure 5.4) than for the ones inside the beam (left column). One can also see that for narrower beams, the low-energy part is placed much higher in comparison to the peak of the primary spectrum. This is especially noticeable inside the beam. Table 5.1 summarizes the three measures for these cases. Where the fraction of low energy electrons to the total does not always vary by a very large factor between cases, the slope and especially the fraction of between the 25 keV point and the peak show large differences.

5.3.2 Energy spectrum

We use two different initial energy spectra, an exponential spectrum with a cutoff at 7.3 MeV, and a spectrum corresponding to a leader potential drop of 60 MV. These initial spectra were shown in Figure 4.5a. All other parameters are kept the same. The source altitude is 12 km, and the beam width is 30°. We can see in Figure 5.5 how the fraction of secondary photons is dramatically lower for the 60 MV spectrum, which is softer than the exponential spectrum. It follows that both the fraction of low-energy to total and 25 keV to peak are very low in this case. In fact, with less than one low-energy ($<$ 30 keV) photon per thousand photons (see Table 5.2), it would be very difficult to observe the low-energy photons at all. Changing the initial conditions also changes the amount of photons that reach satellite altitude. In this case, only 0.6 photons from a 60 MV spectrum would reach space for each 1 photon from a 7.3 cutoff spectrum, adding to the observational difficulty of softer initial spectra in general.

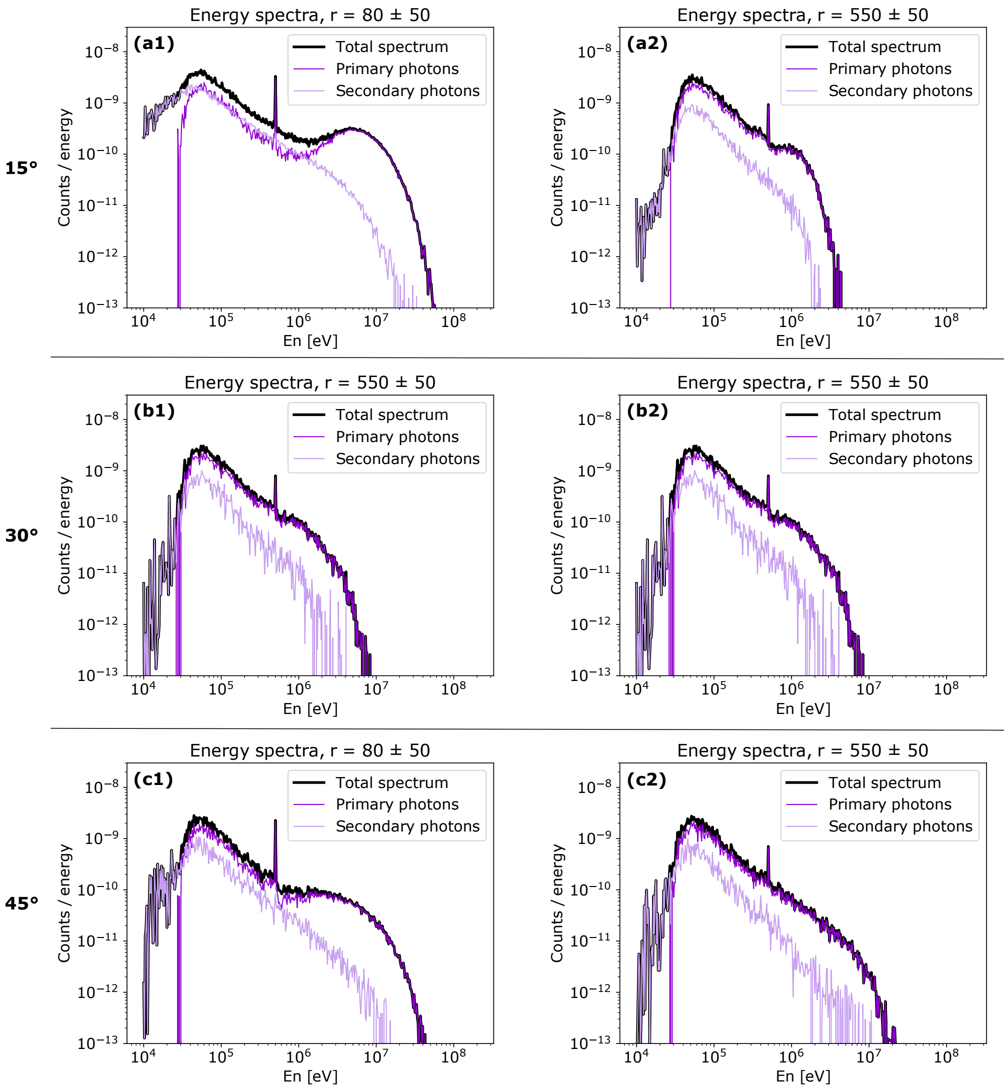

Fig. 5.4: Primary (dark purple) and secondary (lavender) photon spectra for TGFs sourced width different initial beam widths. Each row corresponds to one angle; 15° (a), 30° (b),and 45° (c). The spectra are shown within the beam of the TGF (left column, marked 1), and outside (right, marked 2).

Initial spectrum	Radius	Low-energy-to-total	Slope	25-keV-to-peak
7.3 keV	80 ± 50 km	0.00376	2.60	0.11817
	550 ± 50 km	0.00201	5.91	0.01612
60 MV	80 ± 50 km	0.00098	3.98	0.02491
	550 ± 50 km	0.00049	4.81	0.00388

Table 5.2: Measures of secondary photon spectrum for different initial photon spectra, an exponential spectrum with a cutoff at 7.3 MeV, and one corresponding to a leader potential drop of 60 MV.

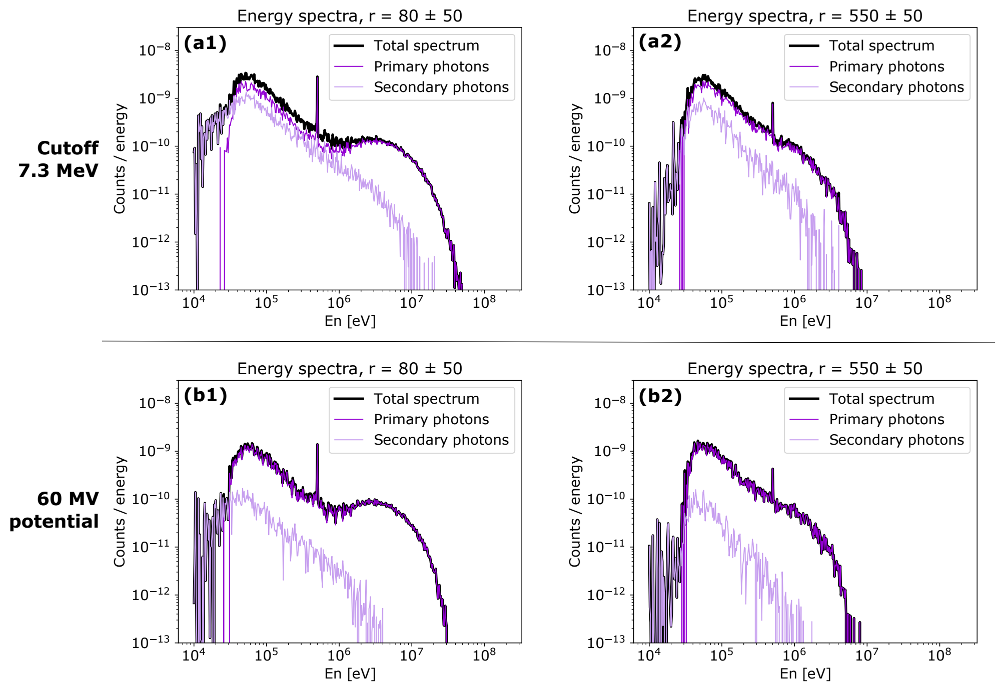

Fig. 5.5: Primary (dark purple) and secondary (lavender) photon spectra for TGFs with different initial energy spectra. The top row (a), is an exponential spectrum with a cutoff at 7.3 MeV, while the bottom row (b) is from a spectrum corresponding to a leader potential drop of 60 MV. The spectra are shown within the beam of the TGF (left column, marked 1), and outside (right, marked 2).

5.3.3 Source altitude

The final parameter we have studied is the source altitude. In Figure 5.6, one can see the resulting energy spectra. The main visual difference here is in fact only the noise level. More photons reach satellite from 15 km than from 12, as they have less air to pass through on average, making a smoother distribution. Both the fraction of low-energy photons to total number of photons and the fraction of the 25-keV point to the peak are remarkably similar (Table 5.3). The difference in the slope might be explained by the noise level of the 12 km case distorting the line fit. It could also be an effect the longer propagation distance causing more of the lowest energy photons to be absorbed in the atmosphere. The difference in slope is in any case relatively small, and would probably be difficult to observe in practice. We can therefore conclude that the source altitude has little to no effect on the fraction of secondary photons.

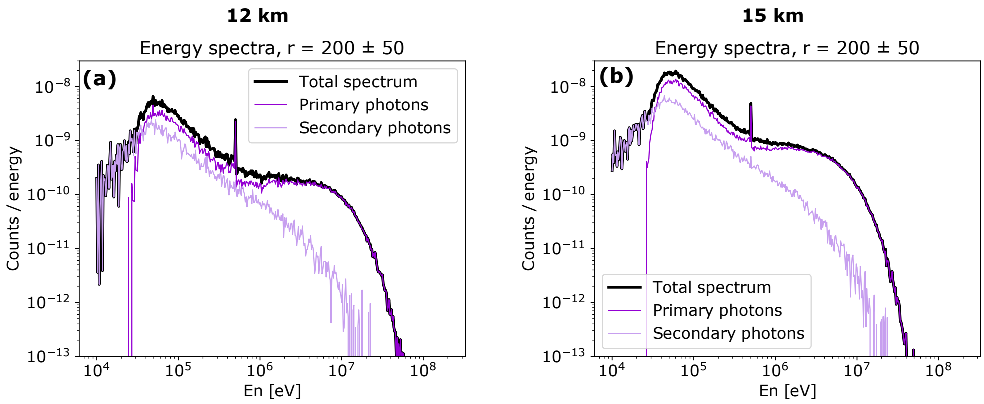

Fig. 5.6: Primary (dark purple) and secondary (lavender) photon spectra for TGFs sourced at 12 km (a) and 15 km (b).

Source altitude	Radius	Low-energy-to-total	Slope	25-keV-to-peak
12 km	200 ± 50 km	0.00425	2.54	0.10763
15 km	200 ± 50 km	0.00458	1.76	0.11692

Table 5.3: Measures of secondary photon spectrum for different source altitudes for the initial TGF.

5.4 Discussion

5.4.1 Behavior of measures

What values one should expect for the three proposed measures – fraction of low-energy photons to total number of photons, fraction of 25-keV point to peak, and the slope of the low energy part of the spectrum – also depends on the observational geometry. As we saw in Tables 5.1 and 5.2, the values differ depending on whether the observer is inside or outside the projected beam of the initial TGF. When plotted as a function of radial distance (r in Figure 5.1), one can see that the two fractions clearly behave differently inside and outside the beam (Figure 5.7). Especially the 25-keV point to peak fraction displays a marked difference, with a high level inside the beam, and a much lower level outside, falling off seemingly linearly with distance. Increasing the beam width of the TGF makes these trends less clear, but still discernible.

We have also seen that the slope seems to increase with radial distance, because the lowest energy photons do not reach as far as those with a slightly higher energy. For the 15° case this increase can be fitted relatively well as a linear increase, given the limited statistics (Figure 5.8). With a 45° beam this linear fit does not hold up statistically, although there seems to still be an increase with distance. This measure does not exhibit any sharp change at the edge of the beam.

In principle, all the presented measures could be used in association with the higher energy part of the spectrum to infer the source geometry and the initial spectrum of TGFs.

5.4.2 Assumptions not accounted for

We know that some TGFs are initiated with a tilt to one side [*Lyu et al.*, 2016; *Mailyan et al.*, 2019], which we have not taken into account in this study. While an interesting additional parameter, the asymmetrical nature of a tilted TGF's "footprint" at satellite altitude makes it difficult to incorporate with the methods we have used here. Introducing a tilt would break the system symmetry, and photons could not be collected over entire rings. This would require many more photons to be kept track of in the simulation to improve the statistics. A tilt might also introduce further ambiguity of the relation of each initial parameter to the prevalence of secondary photons, and would be a good topic for further study.

In most cases, the low-energy part of the spectrum made entirely up from secondary photons only account for about 0.1% – 0.4% of the total photon count. This makes it statistically challenging to observe given currently active instruments, especially with a resolution good enough to implement the proposed techniques. However, new astrophysics missions focused of soft X-rays might provide large effective detection areas as well as a high degree of segmentation to ensure their capability to measure high fluxes [e.g. *Marisaldi* *et al.*, 2015].

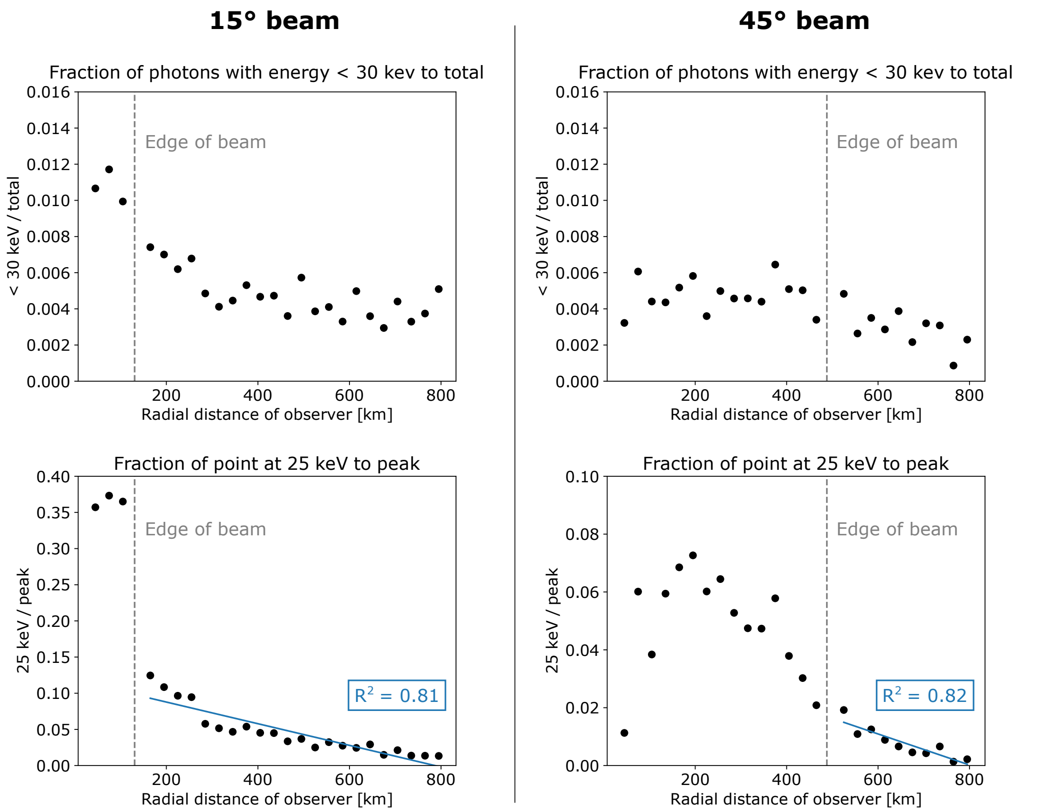

Fig. 5.7: The fraction of low-energy photons to total (top), and 25 keV to peak (bottom) as a function of radial distance of the observer for a TGF with a 15° (left) and 45° (right) beam. For each radius of observation, all photons within ± 15 km are collected. Note that the bottom row does not share a y-axis.

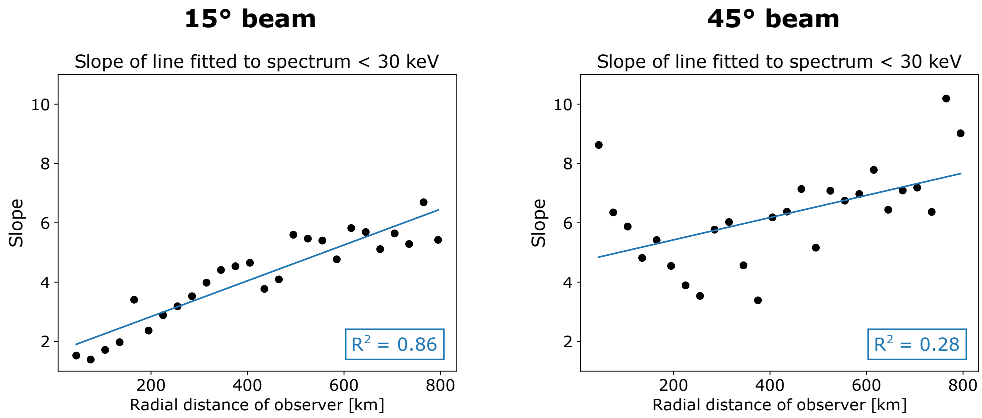

Fig. 5.8: Slope of the < 30 keV part of the energy spectrum as a function of radial distance of the observer for a TGF of beam width 15° (left) and 45° (right). For each radius of observation, all photons within ± 15 km are collected.

5.5 Conclusions

Propagating TGFs cause electrons to be knocked free through interactions with the atmosphere. The bremsstrahlung from these electrons make up a population of photons still energetic enough to reach satellite altitude. Of a given TGF, $\sim$10% – 20% of the photons can be expected to be such secondary photons. However, the only way to tell with certainty whether a photon is a secondary photons, is to look at the part of the energy spectrum below $\sim$30 keV, which is entirely made up of secondary photons.

The fraction of secondary photons, and how their spectrum looks compared to the primary spectrum, changes with the initial conditions of the TGF. As such, they can be used as a way to get more information about their parent TGF. The secondary photons also represent a direct signature of the energy deposited in the atmosphere by a TGF.

We have proposed three measures that can be used to quantify how the energy spectrum of secondary photons relates to the primary spectrum. We have shown how one of them measures may be used to distinguish two cases where the other measures seem similar. We also show how the measures vary with the radial distance of the observer compared to the TGF source. For a detector with sufficient sensitivity in the relevant energy range, this might in the future be used to constrain the source properties of observed TGFs.

Chapter 6

Conclusions and Future Work

6.1 Summary

In this thesis, we have used various methods to model TGFs and different kinds of associated electromagnetic emissions over a broad range of energies — from radio to gamma rays. Below, we recall our main findings corresponding to each chapter, followed by our suggestions for future work. We then present a general conclusion of this thesis.

6.1.1 LF radio emissions from TGF sources

We have used a multifluid plasma model to simulate the currents generated by the RREA at a TGF's source. The radio signal from these currents was then propagated using an analytical formulation, validated by an FDTD model. We have found that these currents should be naturally associated with radio emissions in the LF frequency range. The timescale of the signal we obtained is dependent on the timescale of the initial RREA injection. Using a characteristic duration of 15 μs, we get a final signal of similar duration as observations of so-called slow LF pulses. The magnitude of the electric field, the length of the simulation domain, the injection time of seed electrons, and the initial number of electrons all change the shape and amplitude of the signal. This constrains the combinations of parameters which yield results in agreement with observational data.

We based our choices of initial parameters on the scenario of a lightning leader injecting runaway electrons into an electric field over a region of space. The runaway electrons would then cause a RREA to occur. All the cases presented in Chapter 3 were in physical agreement with this scenario, meaning the scenario is compatible with observations of TGF-associated slow LF pulses.

This study would benefit from future work exploring the full extent of physically valid values of the parameter space. We have performed simulations varied around values we find reasonable for a case that gives good agreement with the available observations of slow LF pulses, but there might be other combinations of initial parameters which could produce equally good results. This is a non-trivial task, as the parameters are all interconnected, and making large changes to one of them requires a re-calibration of the others to get a system which sustains currents over the needed timescale. This work will also be extended to higher frequency emissions directly produced by relativistic electrons to cover a broader range of radio emissions from LF to UHF.

6.1.2 Downward-directed TGFs

While most TGFs are observed by satellites, some have also been detected on ground. We have modeled TGFs beamed in a downward direction using a Monte Carlo model for photon propagation through the atmosphere. We found that despite the differences in distance traveled by the photons in upward and downward TGFs, the time dispersion seen in the impulse responses of TGFs measured at satellite altitude and at ground share a steep peak lasting only microseconds. If pulses of duration shorter than 10 μs with tens of microseconds separation occur in the production of TGFs as observed from the ground, they should be observable from space, given instrumentation with sufficient time resolution.

We also found that most TGF beaming geometries can be uniquely identified by the mean and standard deviation of the detections' position along the tilt axis. This demonstrates the great potential of arrays of evenly spaced ground-based gamma-ray detectors to establish the TGF source position and geometry, when used in combination with lightning mapping. The number of photons arriving at the ground is also heavily dependent on the photons' initial energy spectrum. This may be a source of error when evaluating the number of photons at the source. *Abbasi et al.* [2018] estimate their observations to correspond to $10^{12} - 10^{14}$ initial photons, presumably lower than that forming TGFs observed from space. This could be consistent with a burst of gamma rays produced by lightning leaders forming potential drops of 60 MV.

Future work combining these techniques with observations from the Telescope Array or similar detectors, along with radio detection capability such as interferometer [*Belz et al.*, 2020] and LF magnetic coil antennas (see Chapter

3) would be of great interest.

6.1.3 Low-energy X-rays from TGFs

We have expanded the Monte Carlo model we used for the study on downward TGFs to account for the creation of free electrons by a propagating TGF, and the bremsstrahlung from these electrons. This bremsstrahlung makes up a population of photons still energetic enough to reach satellite altitude. In fact, we find that ~10% – 20% of the photons of a TGF can be expected to be such secondary photons, depending on its initial parameters. The only photons that can be determined to be secondary with certainty are the ones with energy below ~30 keV. Secondary photons can be used as a way to get more information about their parent TGF, because the fraction of secondary photons and how their spectrum looks compared to the primary spectrum changes with the initial conditions of the TGF. Secondary photons also represent a direct signature of the energy deposited in the atmosphere by a TGF.

We have proposed three measures to quantify how the energy spectrum of secondary photons relates to the primary spectrum; the fraction of photons of energy < 30 keV to the total number of photons, the slope of a line fitted to the part of the energy spectrum below 30 keV, and the fraction between the value of this line at 25 keV and the peak of the total spectrum. We have shown how one of the measures may be used to distinguish two cases where the two others seem similar. We also show how the measures vary with the radial distance of the observer compared to the TGF source. For a detector with sufficient sensitivity in the relevant energy range, this might in the future be used to constrain the source properties of observed TGFs.

In the future, including the tilt of the initial TGF as a parameter would be an interesting addition to this study. Future missions with better observing capabilities in the relevant part of the energy spectrum could benefit from the application of the suggested measures to their data. As an example, the astrophysics mission project Large Observatory for X-ray Timing (LOFT) submitted to ESA's Cosmic Vision M4 call for proposals might have a sufficient effective area and segmentation for the presented methods to be used.

6.2 General conclusion

While much has been discovered about the properties of TGFs since their discovery in 1994, many others are unexplored, still unknown, or up for debate. Most notably, there is no consensus on the mechanism starting the RREA responsible for TGF production.

More accurate information on the TGF's geometry, source location and initial energy spectrum places constraints on the models proposed to explain their production mechanism. Because the number of TGF observations is still somewhat sparse, and because the information possible to extract from each observation is limited by its photon count, using modeling to provide techniques for further distinction of results is important. In the studies presented in Chapters 4 and 5, we have provided such techniques for two different scenarios.

TGFs are not an isolated phenomenon — their production and propagation cause secondary physical effects. Such effects prove a valuable addition to direct observations of the TGFs themselves. We have explored the radio emission from TGF sources and the production of a secondary population of gamma-rays by TGFs in Chapters 3 and 5, respectively. Two quite different effects, which each in their way adds possibilities of obtaining partial information about the TGF source and its properties.

We hope that combining multiple TGF-related effects of different nature, including those discussed in this thesis, will result in solving many of the remaining puzzles in high-energy atmospheric physics.

Bibliography

Abbasi, R. U., et al. (2017), The bursts of high energy events observed by the telescope array surface detector, *Physics Letters A*, *381*, 2565–2572, doi:10.1016/j.physleta.2017.06.022.

Abbasi, R. U., et al. (2018), Gamma Ray Showers Observed at Ground Level in Coincidence With Downward Lightning Leaders, *Journal of Geophysical Research (Atmospheres)*, *123*, 6864–6879, doi:10.1029/2017JD027931.

Belz, J. W., et al. (2020), Observations of the origin of downward terrestrial gamma-ray flashes, *Journal of Geophysical Research: Atmospheres*, *n/a*(n/a), e2019JD031,940, doi:10.1029/2019JD031940.

Berge, N., and S. Celestin (2019), Constraining downward terrestrial gamma ray flashes using ground-based particle detector arrays, *Geophysical Research Letters*, *46*(14), 8424–8430, doi:10.1029/2019GL083252.

Berger, M. J., J. H. Hubbell, S. M. Seltzer, J. Chang, J. S. Coursey, R. Sukumar, D. S. Zucker, and K. Olsen (2010), XCOM: Photon Cross Sections Database, `https://www.nist.gov/pml/xcom-photon-cross-sections-database`, doi:https://dx.doi.org/10.18434/T48G6X, accessed: 2019-03-29.

Berger, M. J., M. Inokuti, H. H. Anderson, H. Bichsel, J. A. Dennis, D. Powers, S. M. Seltzer, and J. E. Turner (2016), Report 37, *Journal of the International Commission on Radiation Units and Measurements*, *os19*(2), NP–NP, doi:10.1093/jicru/os19.2.Report37.

Bourdon, A., V. P. Pasko, N. Y. Liu, S. Celestin, P. Segur, and E. Marode (2007), Efficient models for photoionization produced by non-thermal gas discharges in air based on radiative transfer and the helmholtz equations, *Plasma Sources Science and Technology*, *16*(3), 656–678, doi:10.1088/0963-0252/16/3/026.

Briggs, M. S., et al. (2010), First results on terrestrial gamma ray flashes from the Fermi Gamma-ray Burst Monitor, *Journal of Geophysical Research (Space Physics)*, *115*, A07323, doi:10.1029/2009JA015242.

Celestin, S., and V. P. Pasko (2011), Energy and fluxes of thermal runaway electrons produced by exponential growth of streamers during the stepping of lightning leaders and in transient luminous events, *Journal of Geophysical Research (Space Physics)*, *116*, A03315, doi:10.1029/2010JA016260.

Celestin, S., W. Xu, and V. P. Pasko (2015), Variability in fluence and spectrum of high-energy photon bursts produced by lightning leaders, *Journal of Geophysical Research (Space Physics)*, *120*, 10, doi:10.1002/2015JA021410.

Celestin, S., N. L. Berge, B. G. Mailyan, and M. S. Briggs (2020), Geomagnetic deviation of relativistic electron beams producing terrestrial gamma ray flashes, *Journal of Geophysical Research: Space Physics*, *125*(9), e2020JA027,936, doi:10.1029/2020JA027936.

Coleman, L. M., and J. R. Dwyer (2006), Propagation speed of runaway electron avalanches, *Geophysical Research Letters*, *33*, L11810, doi: 10.1029/2006GL025863.

Cummer, S. A., G. Lu, M. S. Briggs, V. Connaughton, S. Xiong, G. J. Fishman, and J. R. Dwyer (2011), The lightning-tgf relationship on microsecond timescales, *Geophysical Research Letters*, *38*(14), doi:10.1029/2011GL048099.

Cummer, S. A., M. S. Briggs, J. R. Dwyer, S. Xiong, V. Connaughton, G. J. Fishman, G. Lu, F. Lyu, and R. Solanki (2014), The source altitude, electric current, and intrinsic brightness of terrestrial gamma ray flashes, *Geophysical Research Letters*, *41*, 8586–8593, doi:10.1002/2014GL062196.

Cummer, S. A., F. Lyu, M. S. Briggs, G. Fitzpatrick, O. J. Roberts, and J. R. Dwyer (2015), Lightning leader altitude progression in terrestrial gamma-ray flashes, *Geophysical Research Letters*, *42*, 7792–7798, doi:10.1002/2015GL065228.

Dwyer, J., B. Grefenstette, and D. Smith (2008), High-energy electron beams launched into space by thunderstorms, *Geophysical Research Letters - GEOPHYS RES LETT*, *35*, doi:10.1029/2007GL032430.

Dwyer, J. R. (2003), A fundamental limit on electric fields in air, *Geophysical Research Letters*, *30*(20), 2055, doi:10.1029/2003GL017781.

Dwyer, J. R. (2008), Source mechanisms of terrestrial gamma-ray flashes, *Journal of Geophysical Research (Atmospheres)*, *113*, D10103, doi:10.1029/2007JD009248.

Dwyer, J. R. (2010), Diffusion of relativistic runaway electrons and implications for lightning initiation, *Journal of Geophysical Research: Space Physics*, *115*(A3), doi:10.1029/2009JA014504.

Dwyer, J. R., and L. P. Babich (2011), Low-energy electron production by relativistic runaway electron avalanches in air, *Journal of Geophysical Research (Space Physics)*, *116*(A9), A09301.

Dwyer, J. R., and S. A. Cummer (2013), Radio emissions from terrestrial gamma-ray flashes, *Journal of Geophysical Research: Space Physics*, *118*(6), 3769–3790, doi:10.1002/jgra.50188.

Dwyer, J. R., and D. M. Smith (2005), A comparison between monte carlo simulations of runaway breakdown and terrestrial gamma-ray flash observations, *Geophysical Research Letters*, *32*(22), doi:10.1029/2005GL023848.

Dwyer, J. R., et al. (2004), A ground level gamma-ray burst observed in association with rocket-triggered lightning, *Geophysical Research Letters*, *31*, L05119, doi:10.1029/2003GL018771.

Dwyer, J. R., D. M. Smith, and S. A. Cummer (2012), High-Energy Atmospheric Physics: Terrestrial Gamma-Ray Flashes and Related Phenomena, *Space Science Reviews*, *173*, 133–196, doi:10.1007/s11214-012-9894-0.

Dwyer, J. R., M. M. Schaal, E. Cramer, S. Arabshahi, N. Liu, H. K. Rassoul, J. D. Hill, D. M. Jordan, and M. A. Uman (2012), Observation of a gamma-ray flash at ground level in association with a cloud-to-ground lightning return stroke, *Journal of Geophysical Research: Space Physics*, *117*(A10), doi:10.1029/2012JA017810.

Enoto, T., et al. (2017), Photonuclear reactions triggered by lightning discharge, *Nature*, *551*, 481–484, doi:10.1038/nature24630.

Fishman, G. J., et al. (1994), Discovery of Intense Gamma-Ray Flashes of Atmospheric Origin, *Science*, *264*, 1313–1316, doi:10.1126/science.264.5163.1313.

Foley, S., et al. (2014), Pulse properties of terrestrial gamma-ray flashes detected by the Fermi Gamma-Ray Burst Monitor, *Journal of Geophysical Research (Space Physics)*, *119*, 5931–5942, doi:10.1002/2014JA019805.

Gjesteland, T., N. Østgaard, A. B. Collier, B. E. Carlson, M. B. Cohen, and N. G. Lehtinen (2011), Confining the angular distribution of terrestrial gamma ray flash emission, *Journal of Geophysical Research (Space Physics)*, *116*, A11313, doi:10.1029/2011JA016716.

Gurevich, A. V., G. M. Milikh, and R. Roussel-Dupre (1992), Runaway electron mechanism of air breakdown and preconditioning during a thunderstorm, *Physics Letters A*, *165*, 463–468, doi:10.1016/0375-9601(92)90348-P.

Hare, B. M., et al. (2016), Ground-level observation of a terrestrial gamma ray flash initiated by a triggered lightning, *Journal of Geophysical Research (Atmospheres)*, *121*, 6511–6533, doi:10.1002/2015JD024426.

Ihaddadene, M. A., and S. Celestin (2015), Increase of the electric field in head-on collisions between negative and positive streamers, *Geophysical Research Letters*, *42*(13), 5644–5651, doi:10.1002/2015GL064623.

Lehtinen, N. G. (2000), Relativistic runaway electrons above thunderstorms, Ph.D. thesis, Stanford University.

Lu, G., et al. (2010), Lightning mapping observation of a terrestrial gamma-ray flash, *Geophysical Research Letters*, *37*(11), doi:10.1029/2010GL043494.

Lyu, F., et al. (2016), Ground detection of terrestrial gamma ray flashes from distant radio signals, *Geophysical Research Letters*, *43*(16), 8728–8734, doi:10.1002/2016GL070154.

Mailyan, B. G., W. Xu, S. Celestin, M. S. Briggs, J. R. Dwyer, E. S. Cramer, O. J. Roberts, and M. Stanbro (2019), Analysis of individual terrestrial gamma-ray flashes with lightning leader models and fermi gamma-ray burst monitor data, *Journal of Geophysical Research: Space Physics*, *124*(8), 7170–7183, doi:10.1029/2019JA026912.

Marisaldi, M., et al. (2010), Detection of terrestrial gamma ray flashes up to 40 MeV by the AGILE satellite, *Journal of Geophysical Research (Space Physics)*, *115*, A00E13, doi:10.1029/2009JA014502.

Marisaldi, M., et al. (2014), Properties of terrestrial gamma ray flashes detected by AGILE MCAL below 30 MeV, *Journal of Geophysical Research (Space Physics)*, *119*, 1337–1355, doi:10.1002/2013JA019301.

Marisaldi, M., et al. (2015), High-energy radiation from thunderstorms and lightning with the Large Observatory for x-ray Timing (LOFT) mission, in *EGU General Assembly Conference Abstracts*, EGU General Assembly Conference Abstracts, p. 14917.

Marshall, R. A. (2012), An improved model of the lightning electromagnetic field interaction with the d-region ionosphere, *Journal of Geophysical Research: Space Physics*, *117*(A3), doi:10.1029/2011JA017408.

Marshall, R. A., C. L. da Silva, and V. P. Pasko (2015), Elve doublets and compact intracloud discharges, *Geophysical Research Letters*, *42*(14), 6112–6119, doi:10.1002/2015GL064862.

Marshall, T. C., M. P. McCarthy, and W. D. Rust (1995), Electric field magnitudes and lightning initiation in thunderstorms, *Journal of Geophysical Research*, *100*(D4), 7097–7103, doi:10.1029/95JD00020.

McCarthy, M. P., and G. K. Parks (1992), On the modulation of x ray fluxes in thunderstorms, *Journal of Geophysical Research: Atmospheres*, *97*(D5), 5857–5864, doi:10.1029/91JD03160.

Mezentsev, A., N. Østgaard, T. Gjesteland, K. Albrechtsen, N. Lehtinen, M. Marisaldi, D. Smith, and S. Cummer (2016), Radio emissions from double RHESSI TGFs, *Journal of Geophysical Research (Atmospheres)*, *121*, 8006–8022, doi:10.1002/2016JD025111.

Østgaard, N., T. Gjesteland, J. Stadsnes, P. H. Connell, and B. Carlson (2008), Production altitude and time delays of the terrestrial gamma flashes: Revisiting the Burst and Transient Source Experiment spectra, *Journal of Geophysical Research (Space Physics)*, *113*, A02307, doi:10.1029/2007JA012618.

Østgaard, N., T. Gjesteland, R. S. Hansen, A. B. Collier, and B. Carlson (2012), The true fluence distribution of terrestrial gamma flashes at satellite altitude, *Journal of Geophysical Research (Space Physics)*, *117*, A03327, doi:10.1029/2011JA017365.

Pu, Y., S. A. Cummer, F. Lyu, M. Briggs, B. Mailyan, M. Stanbro, and O. Roberts (2019), Low frequency radio pulses produced by terrestrial gamma-ray flashes, *Geophysical Research Letters*, *46*(12), 6990–6997, doi:10.1029/2019GL082743.

Qin, J., S. Celestin, and V. P. Pasko (2011), On the inception of streamers from sprite halo events produced by lightning discharges with positive and negative polarity, *Journal of Geophysical Research: Space Physics*, *116*(A6), doi:10.1029/2010JA016366.

Radiocommunication Sector of ITU (2007), Ground-wave propagation curves for frequencies between 10 kHz and 30 MHz, `https://www.itu.int/rec/R-REC-P.368-9-200702-I/en`, accessed: 2020-10-07.

Rakov, V., and M. Uman (2003), *Lightning: Physics and effects*, Cambridge University Press, Cambridge, United Kingdom.

Shao, X.-M., T. Hamlin, and D. M. Smith (2010), A closer examination of terrestrial gamma-ray flash-related lightning processes, *Journal of Geophysical Research: Space Physics*, *115*(A6), doi:10.1029/2009JA014835.

Smith, D. M., L. I. Lopez, R. P. Lin, and C. P. Barrington-Leigh (2005), Terrestrial gamma-ray flashes observed up to 20 mev, *Science*, *307*(5712), 1085–1088, doi:10.1126/science.1107466.

Smith, D. M., et al. (2011), The rarity of terrestrial gamma-ray flashes, *Geophysical Research Letters*, *38*, L08807, doi:10.1029/2011GL046875.

Smith, D. M., G. S. Bowers, M. Kamogawa, D. Wang, T. Ushio, J. Ortberg, J. R. Dwyer, and M. Stock (2018), Characterizing Upward Lightning With and Without a Terrestrial Gamma Ray Flash, *Journal of Geophysical Research (Atmospheres)*, *123*, 11, doi:10.1029/2018JD029105.

Stanbro, M., M. S. Briggs, O. J. Roberts, E. S. Cramer, S. A. Cummer, and J. E. Grove (2018), A Study of Consecutive Terrestrial Gamma-ray Flashes Using the Gamma-ray Burst Monitor, *Journal of Geophysical Research (Space Physics)*, *123*, 9634–9651, doi:10.1029/2018JA025710.

Stanley, M. A., X.-M. Shao, D. M. Smith, L. I. Lopez, M. B. Pongratz, J. D. Harlin, M. Stock, and A. Regan (2006), A link between terrestrial gamma-ray flashes and intracloud lightning discharges, *Geophysical Research Letters*, *33*(6), doi:10.1029/2005GL025537.

Tran, M. D., V. A. Rakov, S. Mallick, J. R. Dwyer, A. Nag, and S. Heckman (2015), A terrestrial gamma-ray flash recorded at the Lightning Observatory in Gainesville, Florida, *Journal of Atmospheric and Solar-Terrestrial Physics*, *136*, 86–93, doi:10.1016/j.jastp.2015.10.010.

Uman, M. A., D. K. McLain, and E. P. Krider (1975), The electromagnetic radiation from a finite antenna, *American Journal of Physics*, *43*(1), 33–38, doi:10.1119/1.10027.

Wilson, C. T. R. (1924), The electric field of a thundercloud and some of its effects, *Proceedings of the Physical Society of London*, *37*(1), 32D–37D, doi:10.1088/1478-7814/37/1/314.

Xu, W., S. Celestin, and V. P. Pasko (2012), Source altitudes of terrestrial gamma-ray flashes produced by lightning leaders, *Geophysical Research Letters*, *39*, L08801, doi:10.1029/2012GL051351.

Xu, W., S. Celestin, V. P. Pasko, and R. A. Marshall (2017), A novel type of transient luminous event produced by terrestrial gamma-ray flashes, *Geophysical Research Letters*, *44*(5), 2571–2578, doi:10.1002/2016GL072400.

Østgaard, N., et al. (2019), First 10 months of tgf observations by asim, *Journal of Geophysical Research: Atmospheres*, *124*(24), 14,024–14,036, doi:10.1029/2019JD031214.

Nini BERGE

Flashs Gamma Terrestres et émissions électromagnétiques associées; des rayonnements radio aux rayonnements gamma

Les flashs gamma terrestres (TGF) sont d'intenses bouffées de rayonnement gamma, de durées inférieures à la milliseconde, produits dans les champs électriques des nuages d'orage. Les TGF sont déclenchés par un processus connu sous le nom d'Avalanche d'Électrons Runaway Relativistes (RREA), mais le mécanisme exact de production et le contexte général derrière ce processus fait encore débat. Dans cette thèse, nous utilisons différents outils de modélisation afin d'explorer les divers aspects des TGF ainsi que des émissions électromagnétiques qui leur sont associées. Ce faisant, nous abordons un des sujets de recherche les plus récents dans le domaine de la physique atmosphérique des hautes énergies.

Lors de la propagation des RREA, des électrons de basse énergie ainsi que des ions positifs et négatifs sont produits. Ces particules chargées produisent des courants lors de leur mouvement dans le champ électrique de l'orage. Nous modélisons les espèces chargées produites par les RREA, et les émissions radio qui en résultent dans le contexte d'électrons runaway thermiques injectés par un leader d'éclair. Nous trouvons que pour certaines conditions initiales, ces émissions radio correspondent aux « slow LF pulses » qui ont été précédemment observés simultanément avec des TGF. Cela confirme que les slow LF pulses sont en fait générés directement par la source du TGF elle-même, comme cela a été précédemment suggéré. Les slow LF pulses pourront ainsi être utilisés pour déterminer les propriétés caractéristiques des sources de TGF.

Depuis que le Telescope Array (Utah, États-Unis) commence à détecter de particules de haute énergie corrélées avec des éclairs, le nombre de détection depuis le sol a considérablement augmenté. Les observations de TGF depuis le sol représentent un outil complémentaire aux observations satellites. La proximité avec l'évènement et la possibilité d'observer un évènement avec plusieurs détecteurs pourraient révéler de nouvelles informations sur la production des TGF. Nous nous intéressons aux TGF inversés (dirigés vers le sol) en utilisant un modèle Monte Carlo de transport de photon dans l'atmosphère. Les pulses de rayonnement gamma détectés par le Telescope Array s'étendent sur des périodes de quelques centaines de microsecondes, avec des structures temporelles inférieure à 10 μs. Nous prédisons que de telles structures seraient observables aux altitudes de satellites, en supposant une résolution temporelle suffisante. D'autre part, nous démontrons comment différents spectres de sources de TGF mèneraient à différent nombres de photons atteignant le sol, ce qui impacte les conclusions qu'on peut tirer en utilisant les données observationnelles.

Lors de la propagation d'un TGF, le rayonnement gamma qui ionise l'air environnant, produisent ainsi des électrons libres. Ces électrons émettent un rayonnement bremsstrahlung (ici appelé photons secondaires), principalement dû aux collisions avec les noyaux des molécules de l'air. Une partie de ce rayonnement bremsstrahlung sera d'énergie suffisante pour atteindre l'altitude des satellites. Le spectre de ces photons secondaires dépend des propriétés initiales du TGF, et peut être utilisé pour caractériser ces dernières à partir des observations. Les photons secondaires sont également une signature directe de l'énergie déposée dans l'atmosphère par les TGF. Parce qu'ils ne sont pas facilement distinguables des photons du TGF, nous proposons trois mesures pour analyser les résultats liés aux spectres des photons secondaires. De cette façon, nous sommes capables de quantifier les propriétés de TGF de différents spectres initiaux et différentes géométrie de faisceaux.

Dans cette thèse, nous démontrons que la combinaison de divers effets de différentes natures liés aux TGF peut être un outil puissant pour résoudre nombre de questions ouvertes dans le domaine de la physique de l'atmosphère des hautes énergies.

Terrestrial Gamma-ray Flashes and Associated Electromagnetic Emissions; from Radio to Gamma rays

Terrestrial Gamma-ray Flashes (TGFs) are bright, sub-millisecond bursts of gamma rays originating in the electric fields of thunderstorms. TGFs are thought to be initiated by a process known as a Relativistic Runaway Electron Avalanche (RREA), but the exact seeding mechanism and general context behind the process remain debated. In this thesis, we use a range of modeling tools to explore several different aspects of TGFs and associated electromagnetic emissions. In doing so, we address some of the most recent research in the field of high-energy atmospheric physics.

As RREAs propagate, they leave a trail of low-energy electrons and positive and negative ions behind. These populations of charged particles will carry currents as they move in the thunderstorm electric field. We model the charged species left behind by the propagating RREA, and the resulting radio emissions in the context of injection of thermal runaway seed electrons by a lightning leader. We find that for certain initial conditions, these radio emissions match slow LF pulses that have previously been observed concurrently with TGFs. This confirms that the slow LF pulses are generated directly by the TGF source itself, as has been previously suggested. Slow LF pulses may therefore be used to infer characteristic properties of TGF sources.

Until recently, there were only a few ground-based observations of TGFs. Since the Telescope Array in Utah, USA, started reporting detections of high- energy particles correlated with lightning, their number has greatly increased. Ground observations of TGFs represent a valuable addition to space-borne detectors. The proximity to the event and the ability to observe an event with several detectors may reveal new information about the production of TGFs. We study downward directed TGFs using Monte Carlo modeling of photon transport through the atmosphere. The Telescope Array-observed pulses of gamma rays spread over periods of a few hundred microseconds, with time structures of less than 10 μs. We predict such structures to be observable at satellite altitude, given sufficient time resolution. Additionally, we demonstrate how various source spectra would lead to different number of photons reaching ground, which impacts the conclusions one can draw using observational data.

As a TGF propagates, gamma rays will knock electrons free as they inter- act with the surrounding air. These electrons emit bremsstrahlung (here referred to as secondary photons), mainly due to collisions with the nuclei of air molecules. Some of this bremsstrahlung has sufficient energy to reach satellite altitude. The spectrum of secondary photons is dependent on the initial TGF's properties, and can be used to infer these from observations. Secondary photons are also a direct signature of the energy deposited into the atmosphere by TGFs. Because they are not easily separated from the photons of the TGF, we propose three measures to analyze results relating to secondary photon spectra. In this way, we are able to quantify properties of TGFs with different initial energy spectra and beaming geometry.

In this thesis, we demonstrate that the combination of multiple TGF-related effects of different nature can be a powerful tool to solve many of the open questions in high-energy atmospheric physics.

LPC2E, CNRS
3A Avenue de la Recherche Scientifique
45100 Orléans, France